Chemical Engineering Journal 470 (2023) 144088

Contents lists available at ScienceDirect

Chemical Engineering Journal

journal homepage: www.elsevier.com/locate/cej

2D/2D NiTi-LDH/BiOBr photocatalyst with extraordinary NO_x removal under visible light

M.A. Oliva [a], J. Ortiz-Bustos [b], M. Cruz-Yusta [a], F. Martin [c], I. del Hierro [b], Y. Pérez [b,d,*], I. Pavlovic [a], L. Sánchez [a,*]

[a] Departamento de Química Inorgánica, Instituto de Química para la Energía y Medioambiente. Universidad de Córdoba, Campus de Rabanales, E-14014, Córdoba, Spain
[b] Departamento de Biología y Geología, Física y Química Inorgánica, Escuela Superior de Ciencias Experimentales y Tecnología. Universidad Rey Juan Carlos, 28933, Móstoles, Madrid, Spain
[c] Departamento de Ingeniería Química, Facultad de Ciencias, Universidad de Málaga, Campus de Teatinos, E-29071, Málaga, Spain
[d] Advanced Porous Materials Unit, IMDEA Energy Institute, Avda. Ramón y Cajal 3, 28935 Móstoles, Madrid, Spain

ARTICLE INFO

Keywords:
LDH
BiOBr
Photocatalysis
Nitrogen Oxides

ABSTRACT

Many current studies are focused on the development of 2D/2D nanosystems based on non-traditional semiconductors as efficient visible light-active photocatalysts, due to their interesting structural and optical properties. Thus, the charge-separation in heterostructures can be enhanced by boosting the interfacial contact. In this work, robust 2D/2D NiTi/BiOBr composites have been prepared by incorporating a 2D layered BiOBr into NiTi-layered double hydroxides (LDH) for the subsequent study of their photocatalytic action in the control of NO_x pollution. The successful formation of a type-II heterojunction between both semiconductors has been confirmed by several characterization techniques (including XPS, NMR and electrochemical studies), indicating an intimate contact interface that helps enhance the visible light photocatalytic performance of NiTi-LDH. In particular, the NiTi–LDH/BiOBr–0.6 heterojunction, with a more efficient separation of photoinduced carriers, showed exceptional NO removal efficiency under visible light and remarkable robustness for the recycling process.

1. Introduction

The increase in road traffic and industrial activity in urban environments has caused the emission of pollutants to rise into the atmosphere. This has turned air quality into a serious problem on a global scale, leading to thousands of premature deaths per year worldwide [1]. One of the main contributors to these deaths are nitrogen oxide gases (NO_x), also known as the overall amount of nitric oxide (NO) and nitrogen dioxide (NO_2). NO_x gases are classified as primary pollutants and are responsible for adverse effects such as acid rain, photochemical smog, stratospheric ozone depletion and the greenhouse effect on the environment. Moreover, the inhalation of these gases can cause asthma, emphysema or bronchitis in the respiratory system [2]. Although legislative measures have been taken to reduce their impact, the recommended NO_x concentration limits in the atmosphere are frequently exceeded. For that reason, there is a high interest in developing new methodologies to remove the NO_x pollution ($DeNO_x$ action).

From the early 2000 s, numerous studies have focused their attention on semiconductor materials as potential photocatalysts for atmospheric pollution remediation. Thus, photocatalysis is becoming an environmentally friendly effective technology which works under mild conditions using natural sunlight as the incoming energy and water and oxygen as the reactants [3]. In the field of photocatalysis, the research progresses are focused on the search for new materials with enhanced properties an efficient exploitation of visible light, higher mobility of the charge carriers and increased accessibility of the reactant molecules to the active sites [4,5]. In this sense, 2D materials are a new subject of study as photocatalytic systems. This is because 2D nanolayered systems possess extraordinary advantages, such as special optical and electrical properties and higher surface area values, endowing them with a favorable capacity for photocatalytic applications. Some examples of these materials are graphitic carbon nitrides [6,7], perovskites [8] and transition metal dichalcogenides [9,10]. However, to date, no single semiconductor meets all the requirements to be a promising photocatalyst on its own. For this reason, different chemical actions have been proposed, like doping [11], quantum dot functionalization [12,13], creation of electronic heterojunctions [14–16] or structural defects [17].

From above, and with the aim of providing new solutions in the

* Corresponding authors.
E-mail addresses: yolanda.cortes@urjc.es (Y. Pérez), luis-sanchez@uco.es (L. Sánchez).

https://doi.org/10.1016/j.cej.2023.144088
Received 2 March 2023; Received in revised form 30 May 2023; Accepted 10 June 2023
Available online 12 June 2023

application of heterogeneous catalysis for air remediation purposes, it is of interest to propose a new electronic structure based on the BiOX (X = Cl, Br or I) and LDH (layered double hydroxides) 2D inorganic semiconductors coupling. The favorable photocatalytic response of heterojunctions based on LDH and BiOX has previously been reported [18–22], but, to the best of our knowledge, none of them have been employed for photocatalytic processes in air. LDHs are a family of anionic clays represented by the general formula $[M^{II}_{1-x}M^{III}_{x}(OH)_2]^{x+}\cdot A^{n-}_{x/n}\cdot mH_2O]$ where M^{II}, M^{III} are divalent and trivalent cations and A^{n-} can be a large number of inorganic or organic anions, which are located in the interlayer spacing together with molecular water [23]. Due to their particular structure and simple synthesis, layered double hydroxides (LDHs) offer the advantage of easily modifying their chemical composition with a variety of metals, thereby improving their electronic properties and enhancing light harvesting while mitigating electron-hole recombination [24–27]. Thus, our research group has found that LDHs containing transition metal cations are highly efficient for photocatalytic NO_x abatement [25–28] with outstanding selectivity towards the formation of nitrate/nitrite species (>90%). However, the main disadvantage of these compounds is that they exhibit poor efficiencies for NO conversion under visible light alone. On the other hand, the inherent optical and electrical properties of BiOX compounds have promoted great attention for their use as visible-light photocatalysts [29]. These are a family of layered compounds consisting of $[Bi_2O_2]^{2+}$ slides interlayered with double slides of halogen atoms, with a tetragonal structure similar to matlockite (PbFCl) mineral [30]. Because the different ionic radius of Cl, Br and I (0.181, 0.196 and 0.220 nm, respectively) the electrical and optical properties of BiOX compounds are modified. Consequently, their corresponding valence band position, energy band gap, light absorption capability and stability are also affected [31–33]. Among the BiOX class, due to the appropriate position of the valence and conduction bands [34,35], bismuth oxybromide (BiOBr) shows exceptional visible light-driven photocatalytic activity for several reactions such as photodegradation of contaminants [36], photocatalytic inactivation of Escherichia coli bacteria [37], CO_2 reduction to fuels [38] or $DeNO_x$ reaction [29], and excellent mobility of the photogenerated electrons [29,39]. Nonetheless, there is still room for improvement of both the enhancement of the visible light absorption (BiOBr only absorbs below 430 nm) [20] and the efficient suppression of electron-hole recombination [40]. In this sense, some efforts have been made to boost the photocatalytic efficiency of BiOBr in the $DeNO_x$ process. Sun et al. [41] promoted with novel 2D $BiOBr/C_3N_4$ nanojunctions not only the enhancement of the visible-light activity of BiOBr, but also the reduction of the electron-hole recombination. However, this material showed a low efficiency for NO removal (32.7 %). Liu et al. [42] prepared $BiOBr/Bi_{12}O_{17}Br_2$ systems employing different ratios of ethylene glycol (EG) and H_2O. Thus, the system obtained with the ratio of EG and H_2O of 0.8 displayed the highest charge-separation efficiency and the lowest interfacial charge-transfer resistance, reaching a superior photocatalytic NO removal efficiency of 57.3 %. A similar photocatalytic performance of 57 % was observed for the BiOBr/BiOI heterojunction due to its ultrathin structure which generates oxygen vacancies enabling NO_3^- adsorption and, thus, changing the photocatalytic mechanism [43].

In this work, we report a simple method to prepare a new nanolayered heterostructure based on NiTi–LDH/BiOBr as a highly enhanced photocatalyst for air remediation. NiTi-CO_3 layered double hydroxide (NiTi-LDH) was prepared with a 3:1 metal ratio of Ni^{2+}/Ti^{4+}, following the previously reported Aqueous Miscible Organic Solvent Treatment (AMOST) synthesis method [28], assuring the synthesis of a 2D-LDH system with a very high specific surface area. The NiTi/BiOBr composites were prepared via the chemical precipitation method using the previously obtained LDH. The physicochemical properties and the photocatalytic performance of the samples were investigated using multiple characterization techniques. Thanks to the intimate contact of both materials, a good electronic structure with a suitable band location for redox reactions was obtained, favoring light absorption of different wavelengths, and creating new pathways for charge carriers that allow an efficient separation of electron-hole (e^-/h^+) pairs. As a result, the obtained 2D/2D system displays outstanding photocatalytic efficiency under visible light in comparison to the single NiTi-LDH and BiOBr systems. The appealing $DeNO_x$ performance of the obtained materials opens the door to explore LDH based 2D/2D heterostructures as new materials for visible light photocatalytic processes.

2. Materials and methods

2.1. Materials

The chemicals used in the synthesis of the samples were: $NiCl_2\cdot 6H_2O$ (Sigma Aldrich, 98%), titanium isopropoxide, $Ti(O^iPr)_4$ (Sigma-Aldrich, 97%), $Na_2CO_3\cdot 10H_2O$ (PanReac AppliChem), $Bi(NO_3)_3\cdot 5H_2O$ (Alfa Aesar) and KBr (Acros Organics), NaOH (Scharlau), ethanol (PanReac AppliChem, 99.5%) and ethylene glycol anhydrous (Glentham Life Sicences, 99.8%).

2.2. Preparation of photocatalysts

2.2.1. Synthesis of NiTi-LDH and BiOBr

Ni_3Ti-CO_3 LDH (NiTi-LDH) was prepared by the co-precipitation method and modified after the aging stage by the AMOST procedure [28] detailed in Supplementary Information (SI).

BiOBr was synthesized in an aqueous solution of ethylene glycol. Firstly, 6 mmol of $Bi(NO_3)_3\cdot 5H_2O$ was added to 44 mL of ethylene glycol under magnetic stirring until complete dissolution at room temperature. Then, 6 mmol of KBr was dissolved in 44 mL of deionized water and the solution was added dropwise to the bismuth solution. After that, the mixture was magnetically stirred for 3.5 h at room temperature. Finally, the product obtained was filtered and washed with deionized water and ethanol, followed by drying in an oven at 60 °C for 2 h.

2.2.2. Preparation of NiTi/BiOBr composites

The synthesis of NiTi/BiOBr composites was carried out in a two-step process with different NiTi-LDH to BiOBr molar ratio: 0.15, 0.6 and 1.2. Firstly, different amounts of the NiTi-LDH sample (0.125, 0.25 and 0.5 g) were dispersed in 25 mL of ethanol to segregate the LDH nano-layers. In a different vessel, 2 mmol of $Bi(NO_3)_3\cdot 5H_2O$ was dissolved in 25 mL of ethylene glycol and the solution was mixed with the corresponding LDH dispersion. The pH of these mixtures was adjusted to 8.0 using NaOH 0.5 M. Subsequently, a solution of 2 mmol of KBr in 25 mL of decarbonated water was added dropwise. The apparition of a colorless precipitate was observed, and the reaction was stirred-continuously for 3.5 h at room temperature. Finally, the composite NiTi/BiOBr was filtered, washed with water and ethanol, and dried at 60 °C for 2 h. The obtained samples were labelled NiTi/BiOBr-x, x being the NiTi-LDH to BiOBr ratio.

2.3. Characterization techniques

The crystalline structure was characterized by X-ray diffraction (XRD) on a Bruker D8 Discover X-ray diffractometer using a monochromatic Cu-Kα radiation (λ = 1.5406 Å). Fourier Transform Infrared (FT-IR) spectrum analyses were performed in the 450–4000 cm^{-1} region with a PerkinElmer Spectrum Two spectrophotometer in Attenuated Total Reflectance (ATR) mode. Transmission electron microscopy (TEM) morphological images were taken on a Jeol JEM-1400 microscope (accelerating voltage = 200 kV). X-ray photoelectron spectroscopy (XPS) was carried out with a Versaprobe II equipment from PHI provided with a focused monochromatic X-ray source (Al-Ka 1486.6 eV). The X-ray and ultraviolet photoelectron spectrometer (XPS, UPS) was a Thermo Scientific Multilab 2000 fitted with a dual anode (MgKα, AlKα) X-ray source.

Pore microstructure and textural properties were analyzed on a Micromeritics ASAP 2020 instrument. The samples were degassed under vacuum overnight at 90 °C before the analysis and measured at 77.4 K using nitrogen as the adsorbent. Specific surface areas were calculated using the Brunauer-Emmett-Teller (BET) multipoint method from the N_2 adsorption and desorption isotherms and pore size distributions were calculated using the density functional theory (DFT) method applied to the adsorption branch of the isotherms. Diffuse reflectance ultraviolet–visible (DRUV–Vis) spectra were collected from 200 to 800 nm employing a Cary 5000 UV–Vis-NIR spectrophotometer (scan rate = 300 nm·min^{-1}; step = 0.5 nm).

Room-temperature wide-NMR line solid-state $^{47/49}$Ti MAS NMR spectra were acquired on a Bruker Avance III/HD spectrometer with an applied field of 9.4 T and using a 4 mm MAS probe spinning at 10 KHz. ^{1}H MAS NMR spectra were also recorded on a Bruker Avance III/HD spectrometer but using a 2.5 mm double resonance probe at MAS rates of 10, 15, 20, 25, 30 and 35 KHz.

The electrochemical measurements were recorded with a potentiostat/galvanostat Autolab PGSTAT302. Electrochemical impedance spectroscopy (EIS) was carried out with an AC signal of 10 mV amplitude in the frequency range between 10 mHz and 100 kHz in potentiostatic conditions.

Additional information about the characterization techniques is available in SI.

2.4. Photocatalytic activity evaluation

Photocatalytic DeNO$_x$ experiments were carried out in a continuous flow photoreactor with a quartz window containing a 50 × 50 mm quartz sample holder with 250 mg of the powdered sample. The photoreactor was placed inside a light sealed irradiation box (Solarbox 3000e RH) equipped with a Xe lamp with controlled irradiance. Artificial sunlight (25 and 500 W·m^{-2} for UV and visible irradiances, respectively) was used as irradiation. For visible light experiments, a LED lamp (420 nm; 510 W/m^2) was used. The photocatalytic activity was studied simulating urban atmosphere conditions of pollutant concentrations, relative humidity and irradiation intensity. To acquire these conditions zero air and NO gas (NO concentration = 150 ppb; air balanced) was mixed and continuously pumped to the photoreactor (flow rate gas = 0.37 L·min^{-1}). The relative humidity was controlled to 45 ± 5% by passing the air flow through a gas-washing bottle filled with demineralised water. Adsorption − desorption equilibrium among photocatalysts was achieved after passing the air/NO flow in the dark for 10 min, before the irradiation period (60 min) started. The gases from the photoreactor circulated to a chemiluminescent analyzer (Environnement AC 32 M) where the concentration of NO, NO_2 and NO_x was measured. The photocatalytic performance was estimated according to the following DeNOx indexes: E_{NO}, E_{NO2}, E_{NOx} and S (described in SI).

Solid-state emission spectra were carried out on a Perkin-Elmer LS 55 fluorescence spectrometer with a Xe lamp at 350 nm excitation wavelength. The data were collected at every 0.5 nm. Slit widths for excitation and emission were 10 nm. Electron paramagnetic resonance (EPR) spectra were recorded on an EMXmicro spectrometer (Bruker) at room temperature. In-situ diffuse reflectance infrared Fourier transform spectroscopy (DRIFTS) measurements were performed with a FTIR spectrometer (Perkin Elmer Frontier) (see SI).

3. Results and discussion

3.1. Composition and structural characterization

Fig. 1a shows the X-ray diffraction (XRD) patterns for the raw materials and heterostructures. In both raw materials, the peaks identified were those characteristics of BiOBr and NiTi-LDH. To obtain a 2D/2D heterojunction it was previously necessary to delaminate the NiTi-LDH

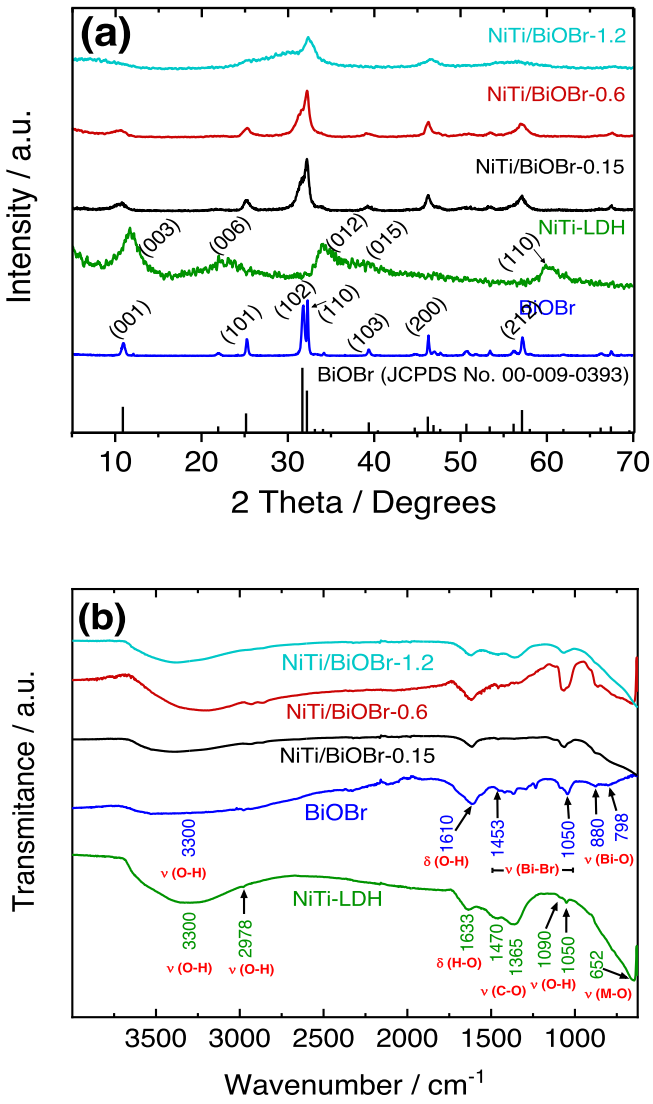

Fig. 1. (a) XRD patterns and (b) FT-IR spectra for the NiTi-LDH, BiOBr and NiTi/BiOBr samples.

sample by using the AMOST process. The characteristic reflections expected for a NiTi-LDH using this procedure were observed [12,28]. The reflections for the (*0 0 3*) and (*0 0 6*) basal planes were located at 2θ ~ 10.9° and 22°, respectively, and those corresponding to (*0 1 2*), (*0 1 5*) and (*1 1 0*) planes were also observed. The low crystallinity of NiTi-LDH is due to its 2D character [12]. During the AMOST procedure the LDH is delaminated and the layer stacking is decreased, resulting in broad and low-intensity basal XRD reflections [44]. On the other hand, the most intense diffraction peaks of BiOBr sample appear at 2θ = 10.9°, 25.3°, 31.9°, 32.3°, 39.4°, 46.2° and 57.2°, which are associated with the (001, 101, 102, 110, 103, 200 and 212) planes of tetragonal BiOBr (JCPDS No. 00–009-0393), respectively.

The XRD patterns corresponding to the composites show the main reflections of BiOBr (*110*, *102*, *110*, *200* and *212* planes) and NiTi-LDH phases (*003* and *012 planes*) indicating that a proper heterostructure was formed. The reflection corresponding to compounds different from the pristine phases was not observed. As the amount of NiTi-LDH is increased the crystallinity of the composite decreases. Particularly, the crystal growth of the BiOBr phase seems to be affected by the presence of LDH, as inferred from the shape of their corresponding XRD peaks indicating a lower crystallinity. It is important to note that LDH also seems to favor the growth of BiOBr on the (1 1 0) direction, as can be seen in the XRD of the NiTi/BiOBr composites for the significant

increase of the intensity ratio of (1 1 0)/(1 0 2) peaks in comparison to the single BiOBr. This could help to enhance the photocatalytic performance of the composites. In this regard, Montoya-Zamora *et al.* demonstrated that the BiOBr sample with (1 1 0) exposed facets exhibited a better photocatalytic activity in the DeNO$_x$ reaction [45]. On the other hand, from the energy dispersive X-ray elemental analysis (EDX) analysis (Fig. S1), the Ni/Ti = 3.0; Bi/Br = 1.0 and Ti/Br = 0.15, 0.6 and 1.2 atomic ratios were found for the samples NiTi/BiOBr-0.15, NiTi/BiOBr-0.6 and NiTi/BiOBr-1.2, respectively. Additionally, the EDX images corresponding to a mapping of the Bi, Br, Ni and Ti elements reveal that they are fully dispersed in the sample, which is indicative of a high degree of homogeneity in the heterojunction (Fig. S1). In the same way, the EDX analysis on HRTEM images confirms the good interconnection between the NiTi-LDH and BiOBr systems in the NiTi/BiOBr composites (Fig. S2).

The FT-IR spectra of studied samples are shown in Fig. 1b. The spectrum for NiTi-LDH shows two bands around 3300 and 1633 cm^{-1}, corresponding to O-H stretching vibrations and the H-O-H bending vibration of the interlayer water molecule, respectively. The bands at 1470 and 1365 cm^{-1} can be assigned to the carbonate located in the interlayer space while those appearing at 2978, 1090 and 1050 cm^{-1} are associated to traces of the ethanol molecules used in the AMOST delamination process which remain in the LDH structure [28]. The intense bands appearing at frequencies lower than 900 cm^{-1} correspond to the M-O and HO-M-OH vibrational bending modes [27]. Analyzing the BiOBr spectrum, the peaks between 1000 and 1500 cm^{-1} could be assigned to Bi-Br bonds. Specifically, the peaks at 1050 and 1453 cm^{-1} should be assigned to the symmetric and asymmetric stretching vibration modes of Bi-Br in the BiOBr structure, respectively. The peaks at 880 and 798 cm^{-1} were assigned to the Bi-O bond symmetric stretching vibration [46]. Again, the bands at 3300 and 1610 cm^{-1} were attributed to the presence of water molecules. For the NiTi/BiOBr composites, the spectra show the main peaks corresponding to both NiTi-LDH and BiOBr structures, increasing the intensity of those for LDH from the NiTi/BiOBr-0.15 to the NiTi/BiOBr-1.2 sample.

X-ray photoelectron spectroscopy (XPS) was used to analyse the oxidation states of Bi, Br, Ti and Ni on the surface of the NiTi-LDH, BiOBr and NiTi/BiOBr samples. The main peak at 284.8 eV for the C 1s signal was used to correct the spectra caused by charge effects. Fig. S3a shows the broad peak for the O 1s signal observed in the 528 – 534 eV region, because of different contributions: lattice oxygen in oxides, hydroxyl groups, carbonate, and adsorbed water. The O 1s peak for BiOBr can be deconvoluted in three peaks at 530.0, 531.0 and 532.5 eV (Figure S4), which have been reported as corresponding to lattice oxygen, atoms in the vicinity of oxygen vacancies, and chemisorbed water [47]. As previously reported by our group, the NiTi O 1s can be also deconvoluted in three peaks at 529.5, 531.1 and 532.5 eV [28], which have been assigned to lattice oxygen in metal oxides (M-O-M), hydroxyl groups (M-O-H) and adsorbed water (H-O-H). For the composites, by increasing the amount of NiTi-LDH the peak is broadened to higher binding energy values, characteristic of the presence of hydroxyl groups and water molecules in LDH [28]. For the BiOBr sample, the single signal for Br 3d appears at 69.0 eV (Fig. S3b) while the corresponding doublet for Bi 4f is located at 164.5 and 159.1 eV (Fig. S3c), values characteristic of this oxyhalide [48]. Interestingly, the slight changes in the position and shape of both signals observed in the NiTi/BiOBr samples suggest the existence of chemical interactions between NiTi-LDH and BiOBr. In a detailed analysis, both Bi 4f$_{5/2}$ and Bi 4f$_{7/2}$ peaks can be deconvoluted into two signals with an FWHM of 1.50 eV and a binding energy difference of about 1 eV, Fig. 2. The deconvolution peak for Bi 4f$_{5/2}$ with its center at 158.8 eV would correspond to Bi^{3-x} valence state, and the peak at 160.1 eV to Bi^{3+}, (Fig. 2a). The formation of the low valence state (3-x) in pure BiOBr has been described as a consequence of sub-stoichiometric forms of Bi at the outer side of the particles, and the

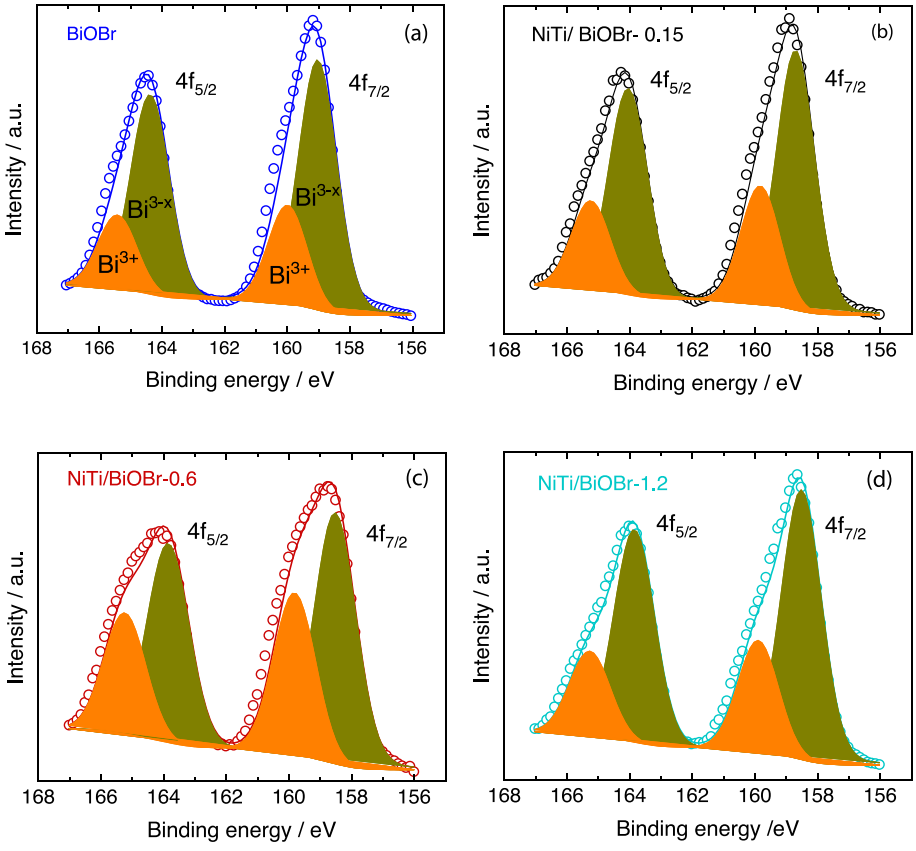

Fig. 2. XPS spectra, Bi 4f region, obtained from the surface of the BiOBr and NiTi/BiOBr samples.

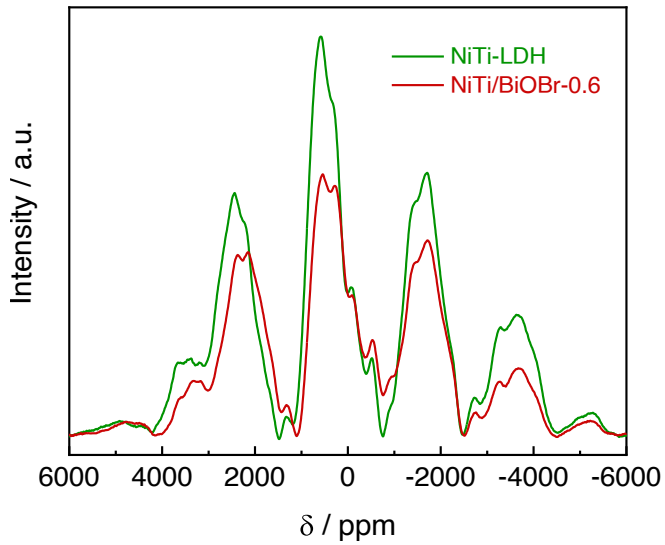

Fig. 3. $^{47/49}$Ti MAS NMR spectra of the NiTi-LDH and NiTi/BiOBr-0.6 samples.

formation of the low oxidation state resulted in the oxygen vacancy on the crystal surface [49,50]. An evolution in the area ratio of both peaks was observed for NiTi/BiOBr samples (Fig. 2b-d), the percentage of Bi^{3+} increasing with the presence of NiTi-LDH and obtaining a maximum Bi^{3+} peak for BiOBr/NiTi-0.6 sample (Fig. S5). The increased presence of Bi^{3+} must be related to the formation of an effective electronic heterojunction. Thus, we could suppose that LDH metals remove electron density from the O-Bi bond, as later demonstrated by electrochemical experiments. In the case of NiTi-LDH, the binding energy for Ni $2p_{3/2}$ (855.4 eV; Fig. S6a) corresponds to hydroxide [28] while the recorded Ti 2p photoelectron peak positions (Fig. S6b; Ti $2p_{3/2}$ = 458.1 eV; Ti $2p_{1/2}$ = 463.7 eV) are the contributions expected from Ti^{4+} ions in octahedral coordination [51]. No significant changes seemed to occur in either of the signals in NiTi/BiOBr samples (Fig. S6c and S6d). For these composites, as BiOBr grew over NiTi-LDH, weaker Ni and Ti signals were registered. In addition, the Ti $2p_{1/2}$ signal overlaps with the more intense signal for Bi 4d. Both items precluded the accurate analysis of possible changes in the Ni 2p and Ti 2p signals in composites.

In order to obtain further information about the structure of the as-prepared 2D-LDH systems, solid-state $^{47/49}$Ti and ^{1}H NMR spectra of NiTi-LDH and NiTi/BiOBr-0.6 were recorded. To the best of our knowledge, there are no reports on solid-state NMR of NiTi-LDH systems. As can be observed in Fig. 3, both spectra display broadened signals with overlapping resonances for ^{47}Ti and ^{49}Ti due to quadrupolar effects [52]. For example, Bastow et *al.* [53] studied the binary NiTi intermetallic compound by $^{47/49}$Ti solid-state NMR and observed a broad Ti resonance at 2707 ppm which was attributed to both ^{47}Ti and ^{49}Ti signals. Padro et al. [54] reported a wide $^{47/49}$Ti SSNMR study of ternary and quaternary titanates with different Ti local environments (TiO_4, TiO_5, and TiO_6), revealing that the chemical shift ranges of these titanium units overlap in some regions. In the $^{47/49}$Ti MAS NMR spectra of NiTi-LDH and NiTi/BiOBr-0.6, similar titanium resonances are observed with a reduction in the intensity of the signals when BiOBr is incorporated on NiTi-LDH. Also, a slight shift to more negative values (>150 ppm) was detected in the spectrum of the NiTi/BiOBr-0.6 sample as compared to the spectrum of NiTi-LDH. This could be due to the titanium species possibly being affected by the growth of BiOBr on NiTi-LDH, revealing an increase in electron density of Ti atoms in the NiTi/BiOBr-0.6 composite and confirming the formation of the heterojunction. In the case of ^{1}H MAS NMR spectra of NiTi-LDH and NiTi/BiOBr-0.6 samples (Fig. S7), a broad signal was observed at a low spinning speed (10 kHz) due to ^{1}H homonuclear dipolar coupling which is caused by the presence of water and hydroxyl groups from NiTi-LDH [55]. Thus, when the spinning speed was increased, a better resolution of ^{1}H resonances was achieved in both samples. In the spectrum of NiTi/BiOBr-0.6, recorded at the highest spinning speed (Fig. 4), the ^{1}H resonances appeared significantly shifted to downfield in comparison to those observed in the spectrum of NiTi-LDH, suggesting that the incorporation of BiOBr leads to an increase of the acidity of the hydroxyl groups of NiTi-LDH, which is consistent with the results seen in $^{47/49}$Ti MAS NMR.

Cyclic voltammetry is a useful technique to obtain qualitative information about the electrochemical processes that occur in the material. In this study, the CV analysis has been performed for pristine BiOBr and NiTi-LDH samples and the composite NiTi/BiOBr-0.6. The electrochemical response of BiOBr recorded in cyclic voltammetry is shown in Fig. 5a, in the potential range from 1.0 to −2.0 V and at different scan rates. After a few cycles of stabilization, one reduction peak was observed at −1.6 V. The oxidation scan showed a weak peak associated at 0.50 V (inset of Fig. 5a). This behavior is comparable to that observed for other bismuth-based materials such as Bi_2O_3 [56], Bi_2WO_6 [57], and $BiPO_4$ [58] using a KOH solution as an electrolyte. As previously published, the cathodic peak is due to the reduction of Bi(III) to Bi metal and the anodic one to the oxidation of Bi metal to Bi(III), the mechanism of reduction being composed of several steps and implying partial dissolution of the solid bismuth material to BiO_2^- ions before electrochemical reduction. The small oxidation peak is due to the location of the bismuth metal near the Bi(0)/solution interface [59]. Additionally, the electrochemical response of NiTi-LDH was recorded under similar experimental conditions (Fig. 5b). The cycle between 0.3 and 0.6 V corresponds to the pseudo-reversible oxidation of Ni(II) sites in LDH lattice (Ni^{2+}−LDH + OH^- $_{electrolyte}$ → (Ni^{2+}_{1-x} Ni^{3+}_x(OH)-LDH + xe^-) as previously observed for NiAl-LDH [60]. On the reverse scan, towards negative potential values, a new process was observed between −1.0 and −0.76 V due to the reduction of Ti(IV) sites (Ti^{4+}−LDH + K^+ $_{electrolyte}$ + xe^-→ ($Ti^{4+}_{1-x}Ti^{3+}_x$(K)-LDH). Previous studies have demonstrated that the contribution of metal active sites on the external surface of LDH containing 3d metal cations ranges from 1.4 % to 10 % of the total charge involved [61], that is, the metal sites located inside the pores are those which govern the electrochemical process. The theoretical model developed by some authors [62–64], establishes that the electrochemical process of a solid compound immobilized on an electrode surface was characterized by mixed ionic/electronic conductivity and the uptake or expulsion of electrons and electrolyte ions taking place at the three-phase junction; where electrode, solid and electrolyte solution meet. Similarly, charge transportation occurs through the LDH layers via electron bouncing between localized metal cations and electrolyte ions across the pores and

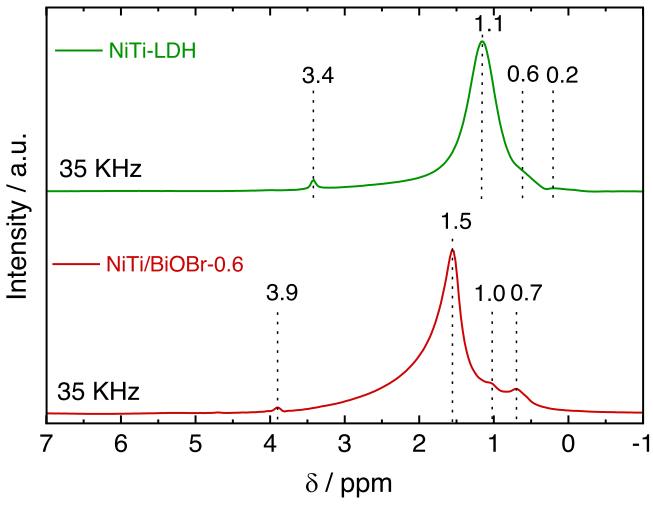

Fig. 4. ^{1}H MAS NMR spectra of the NiTi-LDH and NiTi/BiOBr-0.6 samples acquired at a high spinning speed (35 KHz).

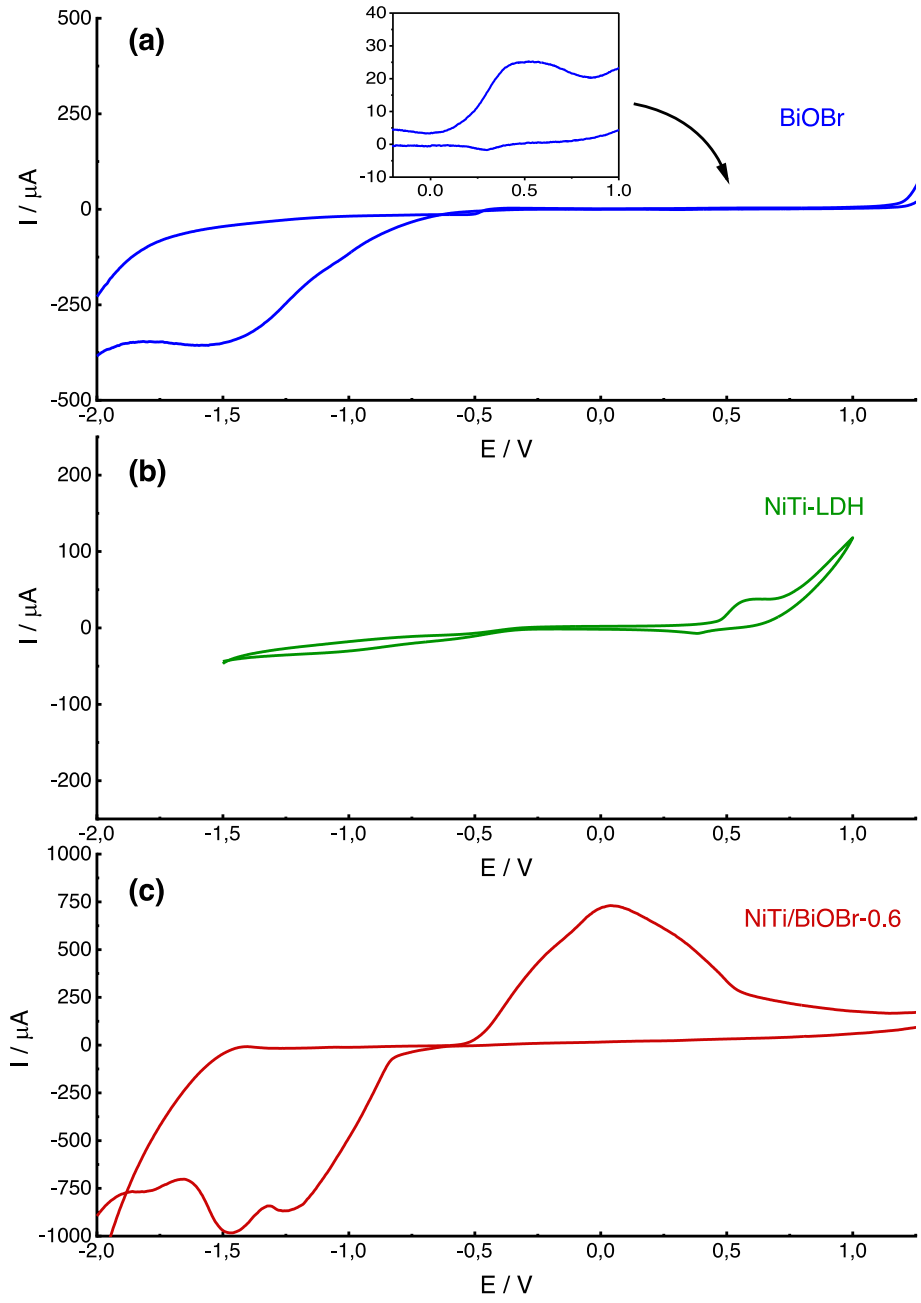

Fig. 5. Cyclic voltammograms obtained for CPE of the (a) pristine BiOBr, (b) NiTi-LDH and (c) NiTi/BiOBr-0.6 samples immersed in aqueous 0.2 M KOH with a reversal potential Vf = -2 V (scan rate 100 mV/s) vs Ag/AgCl(s) KCl (3.0 M) as the reference electrode.

channels of the material to preserve the electroneutrality of the LDH structure, so the electrochemical reaction is governed by a diffusional process of the electrolyte ions (I_p increases linearly with $v^{1/2}$). In addition, Fig. 5c shows the CV plot recorded for the composite NiTi/BiOBr-0.6. The first observation was that the cyclic voltammogram is mainly attributed to the BiOBr phase, and that the synthetic procedure seems to guarantee the growth of the bismuth-based phase on the NiTi-LDH. On the other hand, in comparison to the pristine NiTi-LDH, the current peak intensity measured is so high for the composite material that the overlapping of electrochemical peaks of NiTi-LDH by these new ones cannot be discarded. By assuming that the CV signals are mainly due to the BiOBr phase, some important differences in comparison to pristine BiOBr are also observed as a significant increase in the anodic current peak intensity; thus, the ratio I_{ox}/I_{red} for the BiOBr phase in the NiTi/BiOBr-0.6 sample is much higher than that observed for pristine BiOBr. Furthermore, the difference between anodic and cathodic peak potentials (ΔE_p) decreases which suggests a faster electron transfer rate. Hence, the presence of NiTi-LDH in the composite has a significant effect on reducing the charge transfer resistance and enhancing the reversibility of the electrochemical process. Additionally, the anodic and cathodic peaks with higher current intensity values (Fig. 5c), are situated at lower potentials; the anodic peak associated with the oxidation of Bi metal located near the Bi(0)/solution interface appears at 0.05 V; upon reversal scan two reduction peaks are observed at −1.47 and −1.23 V. These new peaks at higher potential values (less negative) are probably due to the formation of different structural bismuth active species with higher Lewis acid properties, that is, metal centers with higher electron deficiency and hence more easily reduced. The improved electrochemical characteristics can be tentatively attributed to the synergistic effects between Bi(III) and Ni(II)/Ti(IV), by affecting both

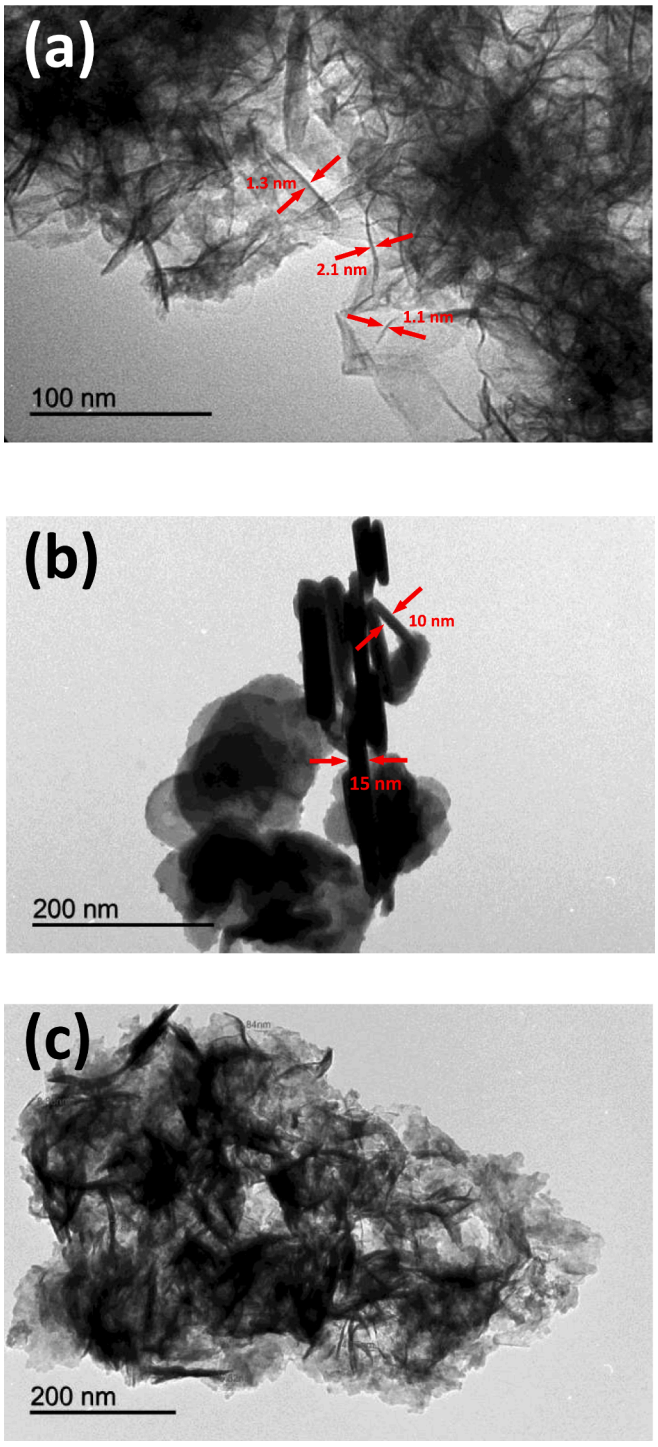

Fig. 6. HRTEM images of the (a) NiTi-LDH, (b) BiOBr and (c) NiTi/BiOBr-1.2 samples.

the electric conductivity of the materials and the chemical properties of the active centers. Miao et al. [65] have observed that the adsorption of an ultrathin layer of bismuth(III) on a platinum electrode greatly increased the electrocatalytic activity of Bi metal/Pt electrode. According to the authors, Bi(0) or Bi(III) species tend to adsorb more of the OH group which is shared by the below adjacent platinum atom to form structures, such as Bi-OH…Pt, highly electroactive in glucose electrocatalytic oxidation. The Pt-O surface is entirely blocked by $Bi(OH)_3$ and/or BiOOH structures, which are highly active in catalysis due to the synergistic action between $Bi(OH)_3$/BiOOH and the below Pt-O. In addition, bismuth blocks the active sites of the platinum avoiding the adsorption of poisoning species. Similarly, the growth of BiOBr on NiTi-LDH may cover the surface of LDH, as well as Bi(III)-O-Ti and Bi(III)-O-Ni structures are formed the electronic density of metallic Bi(III) centers decrease as supported by XPS results and CV measurements (Figs. 5 and 2), and hence an increase of its Lewis acid properties which may greatly enhance its adsorptive properties towards NO molecules. In this sense, the formation of the Bi(III)-O-Ti may increase the electron density of Ti atoms which is in accordance with the results obtained by NMR studies.

To better understand the changes in conductivity occurring during the electrochemical process, electrochemical impedance spectroscopy (EIS) measurements were collected by using a constant-phase element (CPE) from 100 kHz to 0.1 Hz with an amplitude of 10 mV (Fig. S8). The impedance at high and medium frequencies (semicircle) corresponds to the charge-transfer resistance at the interface. The impedance at low frequency (the straight sloping line) is also called Warburg impedance and it is attributed to the Nernst electrolyte diffusion. The inset in Fig. S8 shows an extended view of the Nyquist plots of all photocatalysts, which adopted Randles equivalent circuit as a fitting circuit. According to this, the charge transfer resistance (R_{ct}) is parallel with the CPE [66]. The values of R_{ct}, which were deduced from this plot, are 12.5 Ω, 13.4 Ω, 12.9 Ω, 11.5 Ω and 12 Ω for the NiTi-LDH, BiOBr, NiTi/BiOBr-0.15, NiTi/BiOBr-0.6 and NiTi/BiOBr-1.2 samples, respectively. These results reveal a better electronic conduction in the NiTi/BiOBr-0.6 heterojunction. Also, a lower arc radius of the Nyquist semicircle plot and a smaller slope of the straight line shown by this sample reveal a lower interfacial layer resistance. This suggests that the NiTi/BiOBr-0.6 heterojunction can effectively promote the photogenerated charge carriers transportation and separation efficiency, which indicates a faster interfacial charge transfer ability of the composite in accordance with the results obtained by CV [67].

3.2. *Morphology, textural and optical properties*

The bidimensional morphology of the samples was observed by HRTEM microscopy, Fig. 6. Both samples exhibit a high ratio of lateral size to thickness confirming their 2D nature [68]. NiTi-LDH appear as 2D corrugated nanosheets constituting flower-type particles (Fig. 6a), the characteristic morphology of LDH systems obtained by the AMOST procedure [28,69]. The thickness of the nanosheets is around 1.2 – 2.1 nm indicating that they are constituted by a few LDH monolayers (Fig. S9a). For BiOBr, porous rectangular nanoplates of 100 – 250 nm in size were observed, with the thickness for each nanoplate in the 13–27 nm range (Figs. 6b and S9b). The NiTi/BiOBr composites form 2D/2D heterostructures on which BiOBr nanoplates grew over NiTi-LDH (Fig. 6c). During the synthesis of heterostructure the LDH nanosheets seem to aggregate in bundles (4 – 8 nm thickness; Fig. S9c). As inferred for XRD patterns, the growth of the BiOBr material was influenced by the presence of LDH, and smaller nanoplates appear as rounded particles (20 – 40 nm in size; Fig. S9d).

The nitrogen adsorption–desorption isotherms show the porosity of a sample and help us to know about the availability of the active sites of the photocatalyst towards the reactant molecules. The corresponding tests were carried out to determine the specific surface area and pore structure of the NiTi-LDH, BiOBr, and NiTi/BiOBr samples, Fig. 7. The isotherm of the NiTi-LDH sample corresponds to a type IV isotherm with a hysteresis cycle of type H3 indicative of a uniform mesoporous structure (Fig. 7a). The observed isotherm is characteristic of slit-shaped pores, those accounted from the nanosheets aggregates as observed in HRTEM images. For BiOBr a type II isotherm is found (Fig. 7b) and the uniform arrangement of nanoplates in agglomerates leads to the apparition of a very small H1 hysteresis. For the NiTi/BiOBr composites, as the amount of BiOBr grows over the NiTi-LDH, a transition in the isotherm behavior is observed. The shape of the isotherms changes from a type II to a type IV with an H3 hysteresis cycle becoming more defined as the amount of LDH increases. Concerning the pore volume

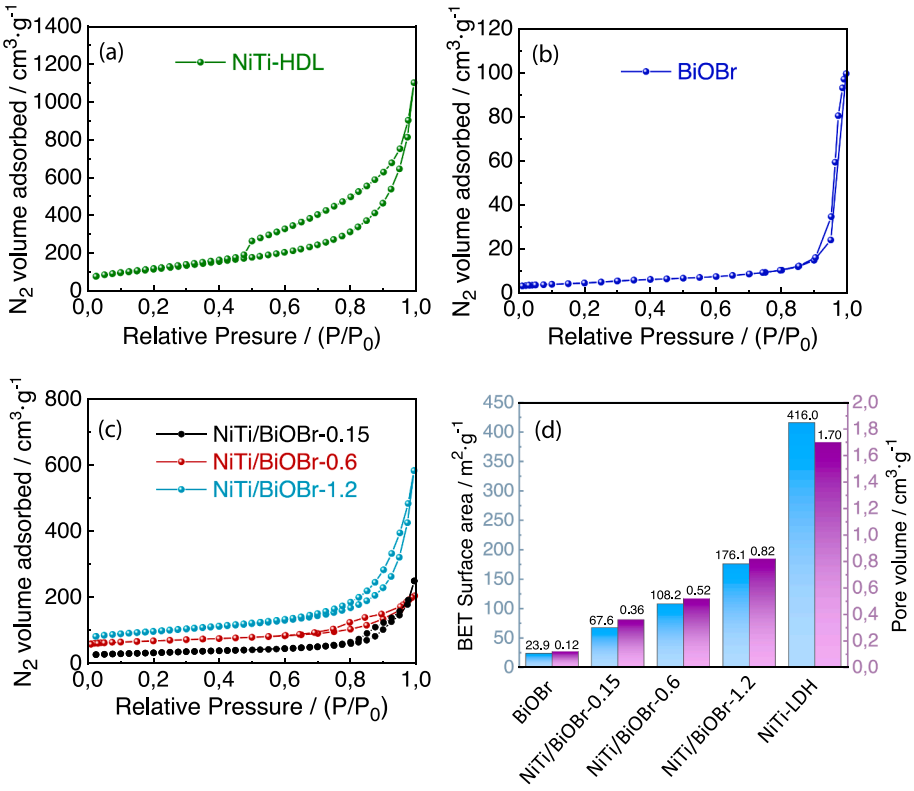

Fig. 7. (a-c) N_2 adsorption–desorption isotherms and (d) BET surface area and pore volume for the NiTi-LDH, BiOBr and NiTi/BiOBr samples.

distribution (Fig. S10), the presence of mesopores is dominant for the NiTi-LDH sample, typical for delaminated LDHs [28], while macropores occur in the case of BiOBr. The pore size distribution for composites covers both mesoporous and microporous regimes, however the shape differs from those observed for the pristine samples. This indicates that an effective growth of BiOBr nanoparticles accounts for the LDH support conforming a new pore microstructure available to the gaseous reactant molecules.

Subsequently, the specific surface area and pore volume values were estimated for each sample (Fig. 7d). Because of the high delamination of the LDH structure and the favorable dispersion of the nanosheets, the NiTi-LDH exhibits a very large specific surface area value (416 $m^2 \cdot g^{-1}$). However, the aggregation of the large nanoplates of BiOBr leads to a low value observed for BiOBr (24 $m^2 \cdot g^{-1}$). The composites exhibit intermediate values which increase with the amount of LDH: 68, 108 and 176 $m^2 \cdot g^{-1}$ for the NiTi/BiOBr-0.15, NiTi/BiOBr-0.6 and NiTi/BiOBr-1.2 samples, respectively. A similar tendency is observed for the pore volume values.

Information about the optical properties of the samples studied was inferred from the diffuse reflectance UV–Vis absorption spectra, Fig. 8a. The NiTi-LDH sample shows an intense adsorption band in the 250 to 400 nm region, associated to ligand-to-metal charge transfer in the octahedral environment ($O^{2-} \rightarrow Ti^{4+}$) [70], with a tail in the visible light region (<500 nm). In addition, the absorbance in the visible region was reinforced by the apparition of a doublet at 675 and 750 nm characteristic of $d - d$ transitions for the Ni(II) ions [71]. BiOBr displays a more limited range of visible light absorption with an absorption edge around 430 nm. The NiTi/BiOBr composites exhibit photo-absorption at wavelengths higher than 400 nm and in the 600–800 nm range implying the possibility of photocatalytic activity under visible light illumination. Band gap values were calculated by plotting the transformed Kubelka-Munk function versus the photon energy, Fig. 8b. Values of 2.50, 2.76, 2.81, 2.87 and 2.54 eV were obtained for the NiTi-LDH, BiOBr, NiTi/BiOBr-0.15, NiTi/BiOBr-0.6 and NiTi/BiOBr-1.2 samples, respectively. Heterojunction formation indicated a shift to higher energy values compared to that of NiTi-LDH.

3.3. Photocatalytic behavior in the $DeNO_x$ process

Photocatalytic $DeNO_x$ tests were performed with the aim of knowing the ability of the samples for air purification purposes. Fig. 9a shows the concentration values of the NO reactant gas flowing in the reaction chamber (150 ppb inlet concentration) at different periods of both dark and light irradiation. In the dark period (first 10 min) the inlet gas concentration remains constant, therefore no physical or chemical interaction seems to occur between the NO gas molecules and the samples or the reactor. Afterward, the reaction chamber was irradiated with UV–Vis light (one hour) and a sudden decay of the concentration values was observed, significant due to the existence of a light induced process. As reported before [5], photons with the appropriate energy promote the transfer of electrons (e^-) in the semiconductor – NiTi-LDH or BiOBr – from the valence band (VB) to the conduction band (CB) with the creation of holes (h^+) in the VB. Once the pair of charges (e^-/h^+) reaches the surface of the photocatalyst, it reacts with water and oxygen adsorbed molecules and produce reactive oxygen radical species (ROS: ·OH, O_2^-). The ROS species are responsible for the oxidation of nitrogen oxide gases which through a complex process are transformed into nitrite and nitrate species [5], thus being removed from air. A steady state of NO elimination was reached for all the samples in the first minutes of light irradiation. At the end of the light irradiation period, outstanding removal efficiency values of $E_{NO} = 69$ % and $E_{NO} = 77$ % were estimated for the NiTi-LDH and BiOBr samples, respectively. Impressively, through the formation of NiTi/BiOBr heterojunctions, complete NO removal is reached by NiTi/BiOBr-0.15 and NiTi/BiOBr-0.6 samples, the NiTi/BiOBr-1.2 sample showing a value of $E_{NO} = 93$ %. The observed $DeNO_x$ performance is not correlated with the specific surface area values measured for each sample, indicating that electronic processes play a key role in the photochemical activity. By way of example, the stability of the NiTi/BiOBr-0.6 sample after the DeNOx test was corroborated as no significant structural, chemical nor morphological

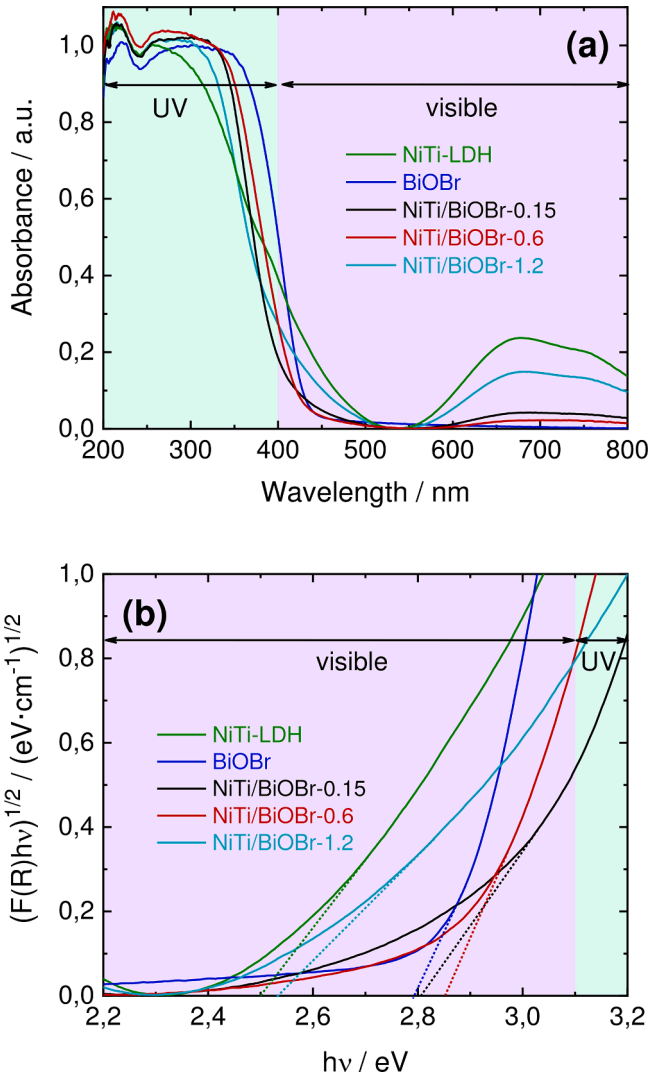

Fig. 8. (a) UV–Vis absorption spectra and (b) Kubelka-Munk transformed function plots for the NiTi-LDH, BiOBr, and NiTi/BiOBr samples.

changes were found (Fig. S11).

NO_2 is one of the intermediates originated during the photochemical oxidation process of NO molecules [5]. It is worth mentioning that NO_2 is highly more toxic than NO [72]; therefore, its release into the atmosphere must be avoided. As expected for the LDHs photocatalysts [25–28,73,74], Figure S12 shows a very low emission of NO_2 (~4 ppb; E_{NO2} = 8 %) during the $DeNO_x$ test when using NiTi-LDH. On the contrary, values of 27 ppb of NO_2 are measured for BiOBr at the end of the light illumination period (E_{NO2} = 18 %), values decreasing for NiTi/BiOBr composites as the amount of NiTi increases, confirming the good role of NiTi-LDH in mitigating the NO_2 release. However, the NiTi/BiOBr-0.15 sample exhibits the highest values of NO_2 concentration during the illumination period (E_{NO2} = 27 %). Apart from its poor content in NiTi-LDH, this sample possesses the lowest volume of mesopores (Fig. S10), whose important role in the inhibition of NO_2 release was previously reported [75]. In this sense, the $DeNO_x$ selectivity (S) – defined as the amount of NO molecules removed from air as harmless nitrite/nitrate species – reaches high values for samples with a high NiTi-LDH content (Fig. S13a). Finally, the NiTi/BiOBr-0.6 sample removes the highest amount of NO_x gases (E_{NOx} = 83 %) due to its better balance between NO removal and selectivity values. A similar tendency of E_{NO} and E_{NO2} values was observed when the samples were used under NO 500 ppb inlet concentration (Fig S14). It is worth noting that at this

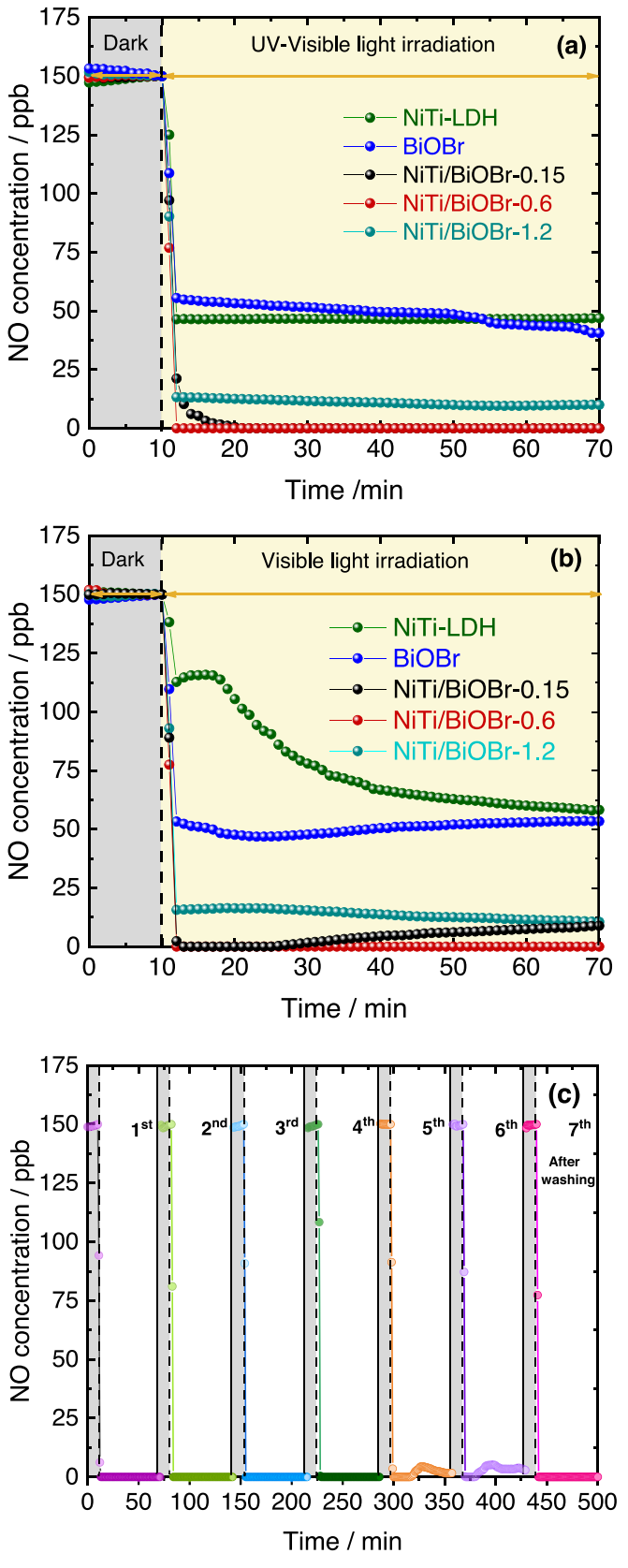

Fig. 9. Nitrogen oxide concentration profile obtained during the photocatalytic NO removal test under (a) UV–Vis and, (b) Vis light on the NiTi-LDH, BiOBr and NiTi/BiOBr samples. (c) Nitrogen oxide concentration profile for each run of the reusability tests for the NiTi/BiOBr-0.6 sample.

three times higher concentration of NO gas, the complete removal of NO was maintained with the same amount of the NiTi/BiOBr-0.6 sample.

Similar $DeNO_x$ tests were carried out under Visible light illumination ($\lambda = 420$ nm), Fig. 9b. As observed for different transition metal LDHs [25–27], the NO removal efficiency was lessened indicating a poorer visible light activity of this photocatalyst. In a similar way, BiOBr and NiTi/BiOBr-0.15 samples exhibited a decreased NO removal value. However, NiTi/BiOBr-0.6 and NiTi/BiOBr-1.2 maintain the extraordinary efficiency for the complete removal of nitrogen oxides (E_{NOx} = 83–84 %; Fig. S13b), validating the importance of the heterojunction formed which works mainly under visible light. The measured E_{NO} index can be considered extraordinary as it clearly surpasses those measured for recently reported $DeNO_x$ photocatalysts acting under visible light, Table S1.

Finally, the $DeNO_x$ photocatalytic process was repeated on different successive runs, Fig. 9c. The complete NO removal was maintained by the NiTi/BiOBr-0.6 sample on each run and only a very slight decrease in efficiency was observed for the 5th and 6th runs. The last accounts by the accumulation of nitrites/nitrate species on the photocatalyst surface, as later commented. Because of its high solubility, these species are easily eliminated when the sample is washed with Milli-Q water after the sixth run. In fact, NO was completely removed again in the following run (7th), indicating the high efficiency and robustness of these photocatalysts.

3.4. Photocatalytic mechanism

Photoluminescence, EPR and DRIFTS experiments assisted in elucidating the photocatalytic mechanism. Fig. 10a shows the photoluminescence (PL) spectra for NiTi-LDH, under an optimized excitation wavelength of 350 nm, along with a comparison to the corresponding spectra to NiTi/BiOBr composites and the BiOBr sample. A doublet PL peak was detected and localized at similar wavelengths in all samples in the 450 – 500 nm range [76]. The NiTi-LDH exhibited the highest PL intensity indicative of the large radiative recombination rate of the electrons and holes in the semiconductor, a competitive pathway with the reaction of the photogenerated charges with O_2 and H_2O molecules to form the ROS species. A decrease in the PL signal was observed for the NiTi/BiOBr samples in comparison with the spectrum of NiTi-LDH which should be associated with the existence of a new deactivation pathway of the photocharges, thanks to the formation of an electronic heterojunction, lessening the recombination of charge carriers. The intensity of the PL signal is lowest for NiTi/BiOBr-0.6 sample indicating an optimal ratio for the photocatalytic performance, as anticipated from the XPS and electrochemistry characterization. These observations are in concordance with the outstanding photocatalytic $DeNO_x$ response observed for the NiTi/BiOBr samples (Fig. 9a and S13a).

EPR measurements were conducted to determine the reactive species involved in the photochemical process. For aqueous solutions, the quartet of peaks DMPO-·OH adduct was only observed for the NiTi-LDH sample after 10 min of light irradiation, but no signal was recorded for BiOBr or NiTi/BiOBr samples (Fig. 10b). On the contrary, for methanolic DMPO solutions, the characteristic sextet of peaks for the trapped $\cdot O_2^-$ radical was observed only for BiOBr or NiTi/BiOBr samples (Fig. 10c). Interestingly, the intensity of the DMPO-·O_2^- adduct signal increases for the composites being the highest in the case of the NiTi/BiOBr-0.6 sample. Therefore, the superoxide radical plays a main role in the photocatalytic process involving the NiTi/BiOBr composites. To confirm the obtained results, scavenger experiments using p-benzoquinone (p-BQ) and *tert*-butanol (t-BOH) to trap superoxide and hydroxyl radical species, respectively, were carried out during De-NOx tests performed with NiTi-LDH, BiOBr, and NiTi/BiOBr-0.6 samples, as shown in Fig. S15. Again, the high production of superoxide radical is confirmed for BiOBr and NiTi/BiOBr-0.6 photocatalysts, as the NO removal is fully inhibited in the presence of p-BQ. On the other hand, NiTi-LDH shows poor ability to produce ROS radicals. Based on these above findings,

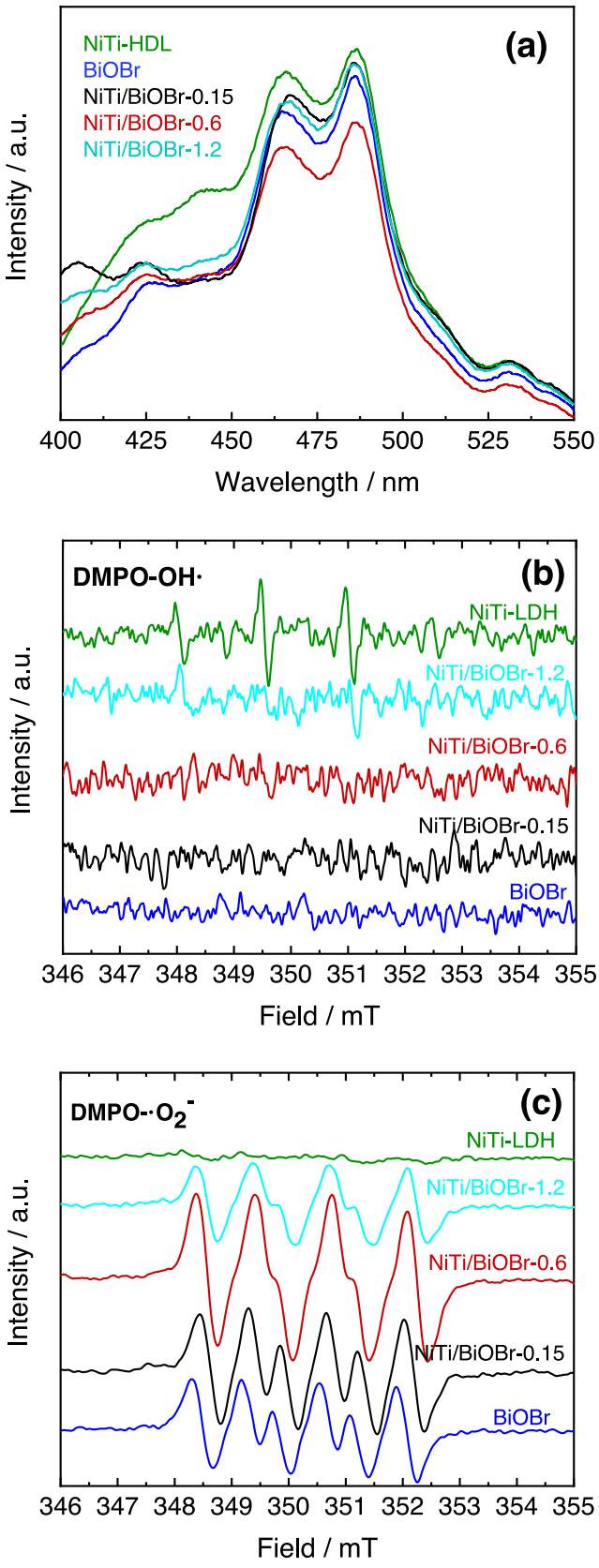

Fig. 10. (a) Photoluminescence (PL) spectra (excitation wavelength = 350 nm) and DMPO spin-trapping EPR spectra in (b) aqueous solution (·OH detection) and (c) methanol solution ($\cdot O_2^-$ detection) for the samples studied.

owing to the effective electronic heterojunction formed at the interface of NiTi/BiOBr composites, the e^-/h^+ recombination was lessened. As a result of a higher availability of charge carriers present on the surface of NiTi/BiOBr, the production of superoxide radicals is favored boosting the performance of these photocatalysts, as observed in $DeNO_x$ tests. On the other hand, even though NiTi-LDH exhibits the highest specific surface area, the obtained data confirm that the poor DeNOx ability observed for this sample was associated with its faster e^-/h^+ recombination and inability to produce superoxide radicals.

To obtain additional information about the photocatalytic mechanism, the interaction between NO molecules and photocatalysts was monitored in-situ using the DRIFTS technique. Previously, the samples were subjected to a pre-treatment process and a background spectrum was recorded. Subsequently, under dark conditions, NO and O_2 flowed through the reaction chamber and sequential spectra were obtained. Fig. 11 shows the spectra obtained for the NiTi-LDH and NiTi/BiOBr-0.6 samples, once the background had been subtracted. As previously reported by our research group[28], NO molecules were easily absorbed on NiTi–LDH being disproportionate to NO^- (1108 cm^{-1}) and NO_2^- species, which ultimately are oxidized to nitrate species in the presence of O_2. In consequence, signals corresponding to nitrite (865, 896, 922, 1371 and 1463 cm^{-1} [77–80] and nitrate (937, 961, 1006, 1057, 1493 and 1540 cm^{-1} [79,81–83] species are observed for the NiTi-LDH sample after 40 min in the dark (Fig. 11a). Afterwards, the sample was irradiated for 60 min. Once light reached the surface of the catalyst, the production of radicals began promoting the oxidation of NO molecules. In consequence, during this period the signals of nitrite and nitrate species increased in intensity and new signals corresponding to these species were observed: 978 and 1036 cm^{-1} for monodentate nitrate [81]; 1144 and 1345 cm^{-1} for bidentate nitrite [77,82]; 1514 and 1572 cm^{-1} for bidentate nitrate [80]. The identification of N_2O_4 (1401 cm^{-1}), as the dimer of NO_2, is in line with the high $DeNO_x$ selectivity of LDH compounds [28].

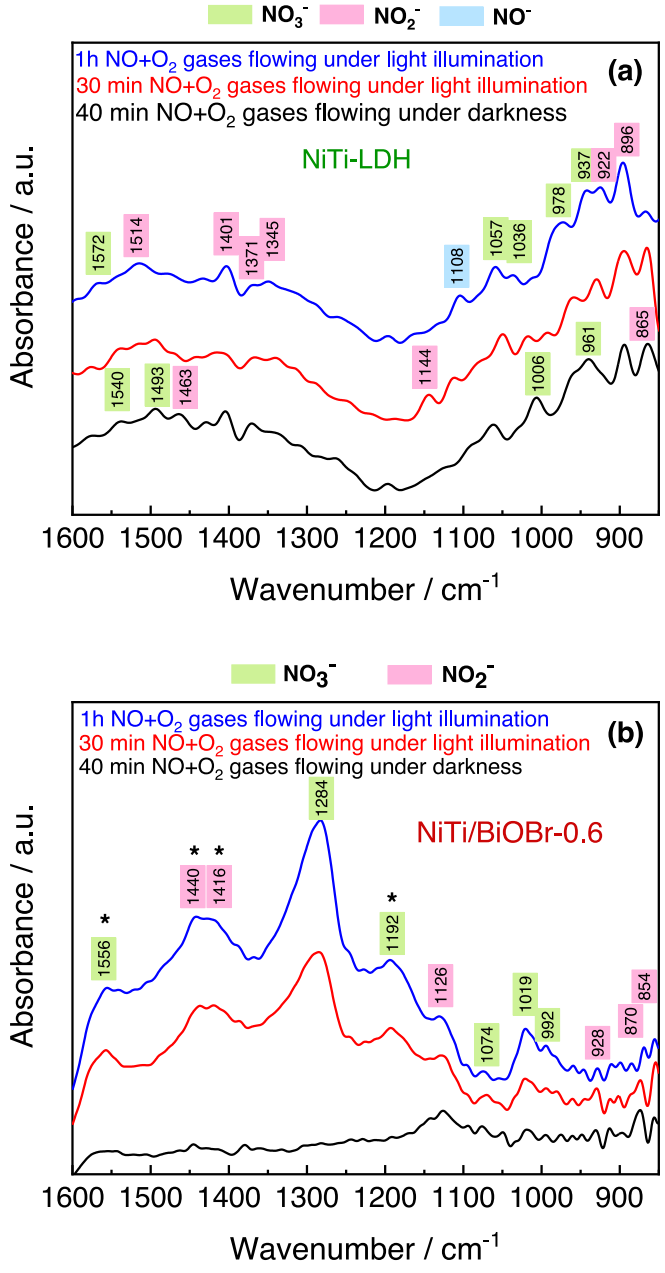

Fig. 11. DRIFT spectra obtained while NO and O2 gases were flowing through the (a) NiTi-LDH and (b) NiTi/BiOBr-0.6 samples in dark conditions and under light illumination.

A similar DRIFTS monitorization was done for the NiTi/BiOBr-0.6 composite. The spectra obtained in the dark period exhibited a similar signature to that of the NiTi-LDH sample. However, during the illumination period, the intensity of the signals was impressively boosted. This means that this photocatalyst exhibits a high ability to produce nitrite (854, 870, 928, 1126, 1416 and 1440 cm^{-1} [28,77,78] and nitrate species (992, 1019, 1074, 1192, 1284 and 1556 cm^{-1} [28,77,82], in other words, to perform the $DeNO_x$ photochemical process. Subsequently, the nitrate signals dominate the spectra, most of them as bidentate or chelate species (marked with an asterisk). Thus, the NiTi/BiOBr-0.6 photocatalyst promotes the complete NO oxidation to nitrates, which are finally stabilized by a bidentate linkage to the surface. Therefore, the reaction mechanism observed by in-situ monitoring confirms the extraordinary ability of the NiTi/BiOBr heterojunctions to perform the NO photochemical oxidation process, in agreement with the results observed from $DeNO_x$ tests (Fig. 9).

Finally, to gain understanding of the photocatalytic mechanism, the Valence Band XPS spectra were acquired for the NiTi-LDH and BiOBr samples (Fig. S16), the valence band (VB) edge being 2.52 and 2.76 eV vs. NHE, respectively (Fig. 12a). Therefore, by considering the previously obtained band gap values (2.50 and 2.87 eV), the conduction band (CB) edge was located at −0.02 eV for NiTi-LDH and −0.11 eV for BiOBr. Meanwhile, the UPS spectrum of both samples allowed the Fermi level to be located at 1.16 eV for NiTi-LDH and 1.46 eV for BiOBr (Fig. S16). Once the redox pair values for the formation of hydroxyl and superoxide radicals are known (Fig. 12), the positioning of the VB and CB edges explains the ability of each sample to produce ·OH or $\cdot O_2^-$ radicals under light irradiation, which is in accordance with EPR measurements (Fig. 10b and 10c). Thus, the position of the CB for BiOBr is needed to form superoxide radicals. However, the energy of the VB edge in both compounds is lower than 2.8 eV, thus preventing the formation of ·OH radicals. On the other hand, the ability of LDHs to form hydroxyl radicals from structural OH^- ($E_{OH^-/\cdot OH}$ = 1.99 eV) has been reported, which explains the DMPO- ·OH adduct signal observed for NiTi-LDH sample (Fig. 10b). When NiTi/BiOBr composites are formed, an electronic contact occurs between both phases matching the Fermi level. Now, the CB and VB edges are shifted to lower values for the BiOBr, being located at −0.41 and 2.46 eV vs. NHE, respectively (Fig. 12b). A type II electronic heterojunction is formed which favors the transfer of the charge carriers generated under light irradiation. Electrons move from BiOBr CB to NiTi-LDH CB and the holes move from NiTi-LDH VB to BiOBr VB. Although this junction effect unfavorably affects the thermodynamics of the involved redox processes, it delays the e^-/h^+ recombination (as inferred from the PL measurements), thus increasing the photocatalytic $DeNO_x$ efficiency of the NiTi/BiOBr photocatalysts (Fig. 9). In fact, the formation of superoxide species is favored on the photocatalyst surface, initiating the oxidation of NO molecules towards nitrite/nitrate species, as monitored by the DRIFTS technique (Fig. 11). This photo-oxidative $DeNO_x$ process involves several steps, which could be summarized in

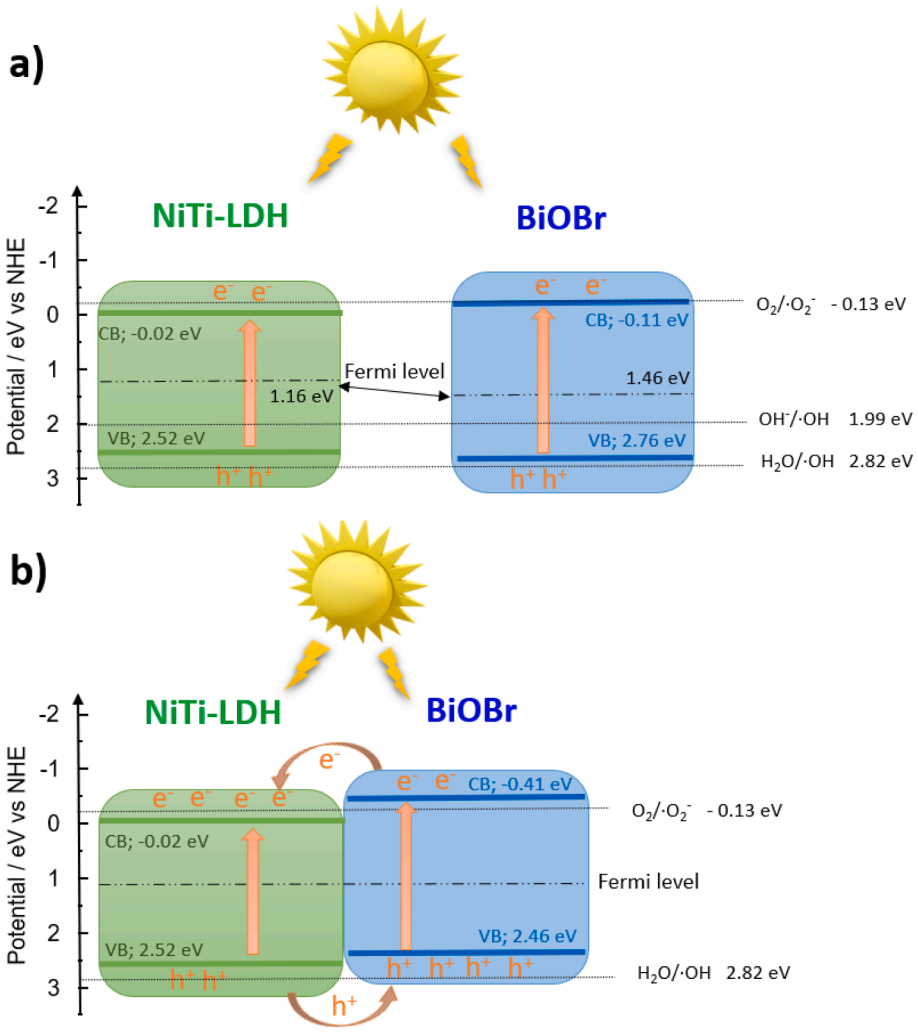

c)

Photo-oxidative DeNO$_x$ process

$$NiTi/BiOBr + h\nu \rightarrow e^- + h^+ \quad (1)$$

$$O_2 + e^- \rightarrow \cdot O_2^- \quad (2)$$

$$NO + \cdot O_2^- \rightarrow NO_3^- \quad (3)$$

$$NO + 2\,H_2O + 3\,h^+ \rightarrow NO_3^- + 4\,H^+ \quad (4)$$

$$O^{2-}_{lattice} + h^+ \rightarrow O^-_{lattice} \quad (5)$$

$$O^-_{lattice} + NO \rightarrow NO_2^- \quad (6)$$

$$2\,NO_2^- + \cdot O_2^- \rightarrow 2\,NO_3^- + e^- \quad (7)$$

Fig. 12. Schematic energy band diagrams for the NiTi-LDH and BiOBr samples, (a) before and (b) after contact, with approximate energy levels with respect to the normal hydrogen electrode (NHE) scale. CB and VB: conduction and valence band edges, respectively. c) Photo-oxidative DeNOx process mechanism.

Fig. 12c [28,84,85]. Additionally, the Mott-Schottky plot of BiOBr sample was performed as a representative sample (Fig. S17). The measurement was recorded at 1 kHz and 10 mV amplitude at potentials from 1 V to −1 V in Na_2SO_4 0.2 M as an electrolyte and by using a calomel electrode as a reference electrode. The flat band potential can be obtained by extrapolation of the M−S tangent line to $1/C^2 = 0$, being −0.5 V (vs. SCE) and −0.256 V in NHE scale for the BiOBr sample. Moreover, the positive slope of the M−S plot confirms that BiOBr is an n-type semiconductor and considering that the CB potential is approximately equals to the flat band potential, the CB value for BiOBr can be located at −0.156 eV. Using the calculated band gap value of BiOBr (i.e. $E_g = 2.87$ eV), the location of the valence band (VB) can be calculated from $E_{CB} = E_{VB} - Eg$, being 2.71 eV. Thus, the E_{CB} and E_{VB} values estimated from Mott-Schottky measurements are in concordance with the results obtained by XPS and UPS measurements.

4. Conclusions

Novel 2D/2D NiTi/BiOBr heterojunctions were successfully prepared by a simple precipitation method under mild conditions. An in-depth study of the textural, optical, morphological and electrochemical properties of these composites confirmed the existence of chemical interactions between NiTi-LDH and BiOBr, which could contribute to the improvement of the optoelectronic properties of 2D/2D heterojunctions. In addition, the incorporation of BiOBr into NiTi-LDH has provided an increase in the electron density of Ti atoms in the heterojunctions, which can greatly enhance their adsorptive properties towards NO molecules. The photocatalytic experiments under visible light revealed that NiTi/BiOBr-0.6 and NiTi/BiOBr-1.2 heterojunctions exhibit a remarkable improvement in the visible light-responsive photocatalytic removal of nitrogen oxides (E_{NOx} = 83–84 %), compared to single NiTi-LDH, BiOBr and other known photocatalysts. In particular, the NiTi/BiOBr-0.6 sample achieved the best balance between NO removal and selectivity, with impressive robustness, reaching high efficiency in repeated photocatalytic cycles.

Based on XPS studies, a type-II heterojunction has been proposed for the hybrid composites before and after efficient contact. This configuration leads to the production of ·OH and $\cdot O_2^-$ radicals and delays the e^-/h^+ recombination increasing the photocatalytic efficiency. PL, EPR and DRIFTS experiments support the effective electronic movement mechanism in the NiTi/BiOBr-0.6 sample, in which the transfer of charge carriers and the formation of superoxide species are favored, being essential for photocatalytic NO_x abatement.

Declaration of Competing Interest

The authors declare that they have no known competing financial interests or personal relationships that could have appeared to influence the work reported in this paper.

Data availability

Data will be made available on request.

Acknowledgements

This work was financed by the Agencia Estatal de Investigación (Spain; MCIN PID2020-117516 GB-I00, PID2020-117832RB-100, RTI2018-094322-B-I00). Mª Ángeles Oliva acknowledges a contract from the Spanish Government (FPU2019/03570).

Appendix A. Supplementary data

Supplementary data to this article can be found online at https://doi.org/10.1016/j.cej.2023.144088.

References

[1] Air quality in Europe 2022 report, European Environment Agency, Luxemburgo, Publications Office of the European Union, (2022). https: //www.eea.europa.eu/publications/air-quality-in-europe-2022, 2022.(accessed 10 February 2023).
[2] A. Chaloulakou, I. Mavroidis, I. Gavriil, Compliance with the annual NO_2 air quality standard in Athens. Required NO_x levels and expected health implications, Atmos. Environ. 42 (2008) 454–465, https://doi.org/10.1016/j.atmosenv.2007.09.067.
[3] J. Ângelo, L. Andrade, L.M. Madeira, A. Mendes, An overview of photocatalysis phenomena applied to NO_x abatement, J. Environ. Manage. 129 (2013) 522–539, https://doi.org/10.1016/j.jenvman.2013.08.006.
[4] H. Dong, G. Zeng, L. Tang, C. Fan, C. Zhang, X. He, Y. He, An overview on limitations of TiO_2-based particles for photocatalytic degradation of organic pollutants and the corresponding countermeasures, Water Res. 79 (2015) 128–146, https://doi.org/10.1016/j.watres.2015.04.038.
[5] M. Cruz-Yusta, M. Sánchez, L. Sánchez, Metal oxide nanomaterials for nitrogen oxides removal in urban environments, C.Maccato, D. Barreca (Eds.), Tailored Functional Oxide Nanomaterials: From Design to Multi-Purpose Applications, Wiley-VCH GmbH,2022, pp.229276. ISBN-13:978-3527347599; https://doi.org/10.1016/j. apsusc.2017.08.192.
[6] Y.J. Yuan, Z. Shen, S. Wu, Y. Su, L. Pei, Z. Ji, M. Ding, W. Bai, Y. Chen, Z.T. Yu, Z. Zou, Liquid exfoliation of g-C_3N_4 nanosheets to construct 2D–2D MoS_2/g-C_3N_4 photocatalyst for enhanced photocatalytic H2 production activity, Appl. Catal. B Environ. 246 (2019) 120–128, https://doi.org/10.1016/j.apcatb.2019.01.043.
[7] W.K. Jo, S. Tonda, Novel CoAl-LDH/g-C_3N_4/RGO ternary heterojunction with notable 2D/2D/2D configuration for highly efficient visible-light-induced photocatalytic elimination of dye and antibiotic pollutants, J. Hazard. Mater. 368 (2019) 778–787, https://doi.org/10.1016/j.jhazmat.2019.01.114.
[8] Z. Dong, S. Su, Z. Zhang, Y. Jiang, J. Xu, NiFe-Layered Double Hydroxides/Lead-free $Cs_2AgBiBr$ 6 Perovskite 2D/2D Heterojunction for Photocatalytic C_O2 Conversion, Inorg. Chem. 62 (4) (2023) 1752–1761.
[9] F. Ma, Y. Wu, Y. Shao, Y. Zhong, J. Lv, X. Hao, 0D/2D nanocomposite visible light photocatalyst for highly stable and efficient hydrogen generation via recrystallization of CdS on MoS_2 nanosheets, Nano Energy. 27 (2016) 466–474, https://doi.org/10.1016/j.nanoen.2016.07.014.
[10] M. Li, Z. Cui, E. Li, Silver-modified MoS_2 nanosheets as a high-efficiency visible-light photocatalyst for water splitting, Ceram. Int. 45 (2019) 14449–14456, https://doi.org/10.1016/j.ceramint.2019.04.166.
[11] B. Wang, D. Chen, N. Li, Q. Xu, H. Li, J. He, J. Lu, Z-scheme photocatalytic NO removal on a 2D/2D iodine doped $BiOIO_3$/g-C_3N_4 under visible-light irradiation, J. Colloid Interface Sci. 576 (2020) 426–434, https://doi.org/10.1016/j.jcis.2020.05.037.
[12] J. Fragoso, A. Pastor, M. Cruz-Yusta, F. Martin, G. de Miguel, I. Pavlovic, M. Sánchez, L. Sánchez, Graphene quantum dots/NiTi layered double hydroxide heterojunction as a highly efficient De-NO_x photocatalyst with long persistent post-illumination action, Appl. Catal. B Environ. 322 (2023), https://doi.org/10.1016/j.apcatb.2022.122115.
[13] Y. Sheng, D. Yi, H.u. Qingsong, W.u. Ting, L.i. Ming, C. Yong, S. Yifan, D.i. Jun, W. Bin, J. Xia, L.i. Huaming, CQDs modified $PbBiO_2Cl$ nanosheets with improved molecular oxygen activation ability for photodegradation of organic contaminants, J. Photochem. Photobiol. A Chem. 382 (2019) 111921.
[14] T.A. Shifa, F. Wang, Y. Liu, J. He, Heterostructures Based on 2D Materials: A Versatile Platform for Efficient Catalysis, Adv. Mater. 31 (45) (2019) 1804828.
[15] J. Hu, D. Chen, Z. Mo, N. Li, Q. Xu, H. Li, J. He, H. Xu, J. Lu, Z-Scheme 2D/2D heterojunction of black phosphorus/monolayer Bi_2WO_6 nanosheets with enhanced photocatalytic activities, Angew. Chemie - Int. Ed. 58 (2019) 2073–2077, https://doi.org/10.1002/anie.201813417.
[16] J. Low, S. Cao, J. Yu, S. Wageh, Two-dimensional layered composite photocatalysts, Chem Commun. 50 (2014) 10768–10777, https://doi.org/10.1039/c4cc02553a.
[17] H. Chi, J. Dong, T. Li, S. Bai, L. Tan, J. Wang, T. Shen, G. Liu, L. Liu, L. Sun, Y. Zhao, Y.-F. Song, Scaled-up synthesis of defect-rich layered double hydroxide monolayers without organic species for efficient oxygen evolution reaction, Green Energy Environ. 7 (5) (2022) 975–982.
[18] J. Xiong, H.Y. Zeng, C.R. Chen, G.F. Xiao, D.S. An, Hierarchical p-n heterostructure BiOI@ZnTi-LDH for Cr(VI) reduction under visible light, J. Alloys Compd. 833 (2020), 154898, https://doi.org/10.1016/j.jallcom.2020.154898.
[19] Y. Cui, J. Ma, M. Wu, J. Wu, J. Zhang, Y. Xu, Q. Liu, G. Qian, Facet-dependent topo-heterostructure formed by BiOCl and ZnCr-LDH and its enhanced visible-light photocatalytic activity, Sep. Purif. Technol. 254 (2021), 117635, https://doi.org/10.1016/j.seppur.2020.117635.
[20] L. Kong, Z. Jiang, T. Xiao, L. Lu, M.O. Jones, P.P. Edwards, Exceptional visible-light-driven photocatalytic activity over BiOBr-$ZnFe_2O_4$heterojunctions, Chem Commun. 47 (2011) 5512–5514, https://doi.org/10.1039/c1cc10446b.
[21] J. Ma, J. Ding, L. Yu, L. Li, Y. Kong, S. Komarneni, BiOCl dispersed on NiFe-LDH leads to enhanced photo-degradation of Rhodamine B dye, Appl. Clay Sci. 109–110 (2015) 76–82, https://doi.org/10.1016/j.clay.2015.02.009.
[22] Y. Ao, D. Wang, P. Wang, C. Wang, J. Hou, J. Qian, A BiOBr/Co-Ni layered double hydroxide nanocomposite with excellent adsorption and photocatalytic properties, RSC Adv. 5 (2015) 54613–54621, https://doi.org/10.1039/c5ra05473g.
[23] M.J. Mochane, S.I. Magagula, J.S. Sefadi, E.R. Sadiku, T.C. Mokhena, Morphology, thermal stability, and flammability properties of polymer-layered double hydroxide (Ldh) nanocomposites: a review, Crystals 10 (2020) 1–26, https://doi.org/10.3390/cryst10070612.
[24] K. Parida, L. Mohapatra, N. Baliarsingh, Effect of Co^{2+} substitution in the framework of carbonate intercalated Cu/Cr LDH on structural, electronic, optical, and photocatalytic properties, J. Phys. Chem. C. 116 (2012) 22417–22424, https://doi.org/10.1021/jp307353f.
[25] F. Rodriguez-Rivas, A. Pastor, G. de Miguel, M. Cruz-Yusta, I. Pavlovic, L. Sánchez, Cr^{3+} substituted Zn-Al layered double hydroxides as UV–Vis light photocatalysts for NO gas removal from the urban environment, Sci. Total Environ. 706 (2020), 136009, https://doi.org/10.1016/j.scitotenv.2019.136009.
[26] A. Pastor, F. Rodriguez-Rivas, G. de Miguel, M. Cruz-Yusta, F. Martin, I. Pavlovic, L. Sánchez, Effects of Fe^{3+} substitution on Zn-Al layered double hydroxides for enhanced NO photochemical abatement, Chem Eng. J. 387 (2020), 124110, https://doi.org/10.1016/j.cej.2020.124110.
[27] J. Fragoso, M.A. Oliva, L. Camacho, M. Cruz-Yusta, G. de Miguel, F. Martin, A. Pastor, I. Pavlovic, L. Sánchez, Insight into the role of copper in the promoted photocatalytic removal of NO using Zn2-xCuxCr-CO3 layered double hydroxide, Chemosphere 275 (2021) 130030.
[28] A. Pastor, C. Chen, G. de Miguel, F. Martin, M. Cruz-Yusta, J.-C. Buffet, D. O'Hare, I. Pavlovic, L. Sánchez, Aqueous miscible organic solvent treated NiTi layered double hydroxide De-NOx photocatalysts, Chem Eng. J. 429 (2022) 132361.

[29] W. Zhang, Q. Zhang, F. Dong, Visible-light photocatalytic removal of NO in air over BiOX (X = Cl, Br, I) single-crystal nanoplates prepared at room temperature, Ind. Eng. Chem. Res. 52 (2013) 6740–6746, https://doi.org/10.1021/ie400615f.

[30] W. Wang, F. Huang, X. Lin, J. Yang, Visible-light-responsive photocatalysts xBiOBr-(1–x)BiOI, Catal. Commun. 9 (2008) 8–12, https://doi.org/10.1016/j.catcom.2007.05.014.

[31] X. Wu, K. Zhang, G. Zhang, S. Yin, Facile preparation of BiOX (X = Cl, Br, I) nanoparticles and up-conversion phosphors/BiOBr composites for efficient degradation of NO gas: oxygen vacancy effect and near infrared light responsive mechanism, Chem Eng. J. 325 (2017) 59–70, https://doi.org/10.1016/j.cej.2017.05.044.

[32] F. Nekouei, S. Nekouei, Comparative evaluation of BiOCl–NPls–AC composite performance for methylene blue dye removal from solution in the presence/absence of UV irradiation: kinetic and isotherm studies, J. Alloys Compd. 701 (2017) 950–966, https://doi.org/10.1016/j.jallcom.2017.01.157.

[33] M. Jahurul Islam, D. Amaranatha Reddy, N.S. Han, J. Choi, J.K. Song, T.K. Kim, An oxygen-vacancy rich 3D novel hierarchical MoS_2/BiOI/AgI ternary nanocomposite: enhanced photocatalytic activity through photogenerated electron shuttling in a Z-scheme manner, Phys. Chem. Chem. Phys. 18 (2016) 24984–24993, https://doi.org/10.1039/c6cp02246d.

[34] M. Referenciado, Bismuth oxyhalides: synthesis, structure and photoelectrochemical activity, AIChE Annu Meet. Conf. Proc. (2019-Novem (2019).), https://doi.org/10.1039/x0xx00000x.

[35] Y. Yang, C. Zhang, C. Lai, G. Zeng, D. Huang, M. Cheng, J. Wang, F. Chen, C. Zhou, W. Xiong, BiOX (X = Cl, Br, I) photocatalytic nanomaterials: applications for fuels and environmental management, Adv. Colloid Interface Sci. 254 (2018) 76–93, https://doi.org/10.1016/j.cis.2018.03.004.

[36] Y. Zhang, P. Cao, X. Zhu, B. Li, Y. He, P. Song, R. Wang, Facile construction of BiOBr ultra-thin nano-roundels for dramatically enhancing photocatalytic activity, J. Environ. Manage. 299 (2021), 113636, https://doi.org/10.1016/j.jenvman.2021.113636.

[37] D. Wu, B. Wang, W. Wang, T. An, G. Li, T.W. Ng, H.Y. Yip, C. Xiong, H.K. Lee, P. K. Wong, Visible-light-driven BiOBr nanosheets for highly facet-dependent photocatalytic inactivation of Escherichia coli, J. Mater. Chem. A. 3 (2015) 15148–15155, https://doi.org/10.1039/c5ta02757h.

[38] L. Ye, X. Jin, C. Liu, C. Ding, H. Xie, K.H. Chu, P.K. Wong, Thickness-ultrathin and bismuth-rich strategies for BiOBr to enhance photoreduction of CO_2 into solar fuels, Appl. Catal. B Environ. 187 (2016) 281–290, https://doi.org/10.1016/j.apcatb.2016.01.044.

[39] K. Sharma, V. Dutta, S. Sharma, P. Raizada, A. Hosseini-Bandegharaei, P. Thakur, P. Singh, Recent advances in enhanced photocatalytic activity of bismuth oxyhalides for efficient photocatalysis of organic pollutants in water: a review, J. Ind. Eng. Chem. 78 (2019) 1–20, https://doi.org/10.1016/j.jiec.2019.06.022.

[40] L. Ye, Y. Su, X. Jin, H. Xie, C. Zhang, Recent advances in BiOX (X = Cl, Br and I) photocatalysts: synthesis, modification, facet effects and mechanisms, Environ. Sci. Nano 1 (2014) 90–112, https://doi.org/10.1039/c3en00098b.

[41] Y. Sun, W. Zhang, T. Xiong, Z. Zhao, F. Dong, R. Wang, W.K. Ho, Growth of BiOBr nanosheets on C_3N_4 nanosheets to construct two-dimensional nanojunctions with enhanced photoreactivity for NO removal, J. Colloid Interface Sci. 418 (2014) 317–323, https://doi.org/10.1016/j.jcis.2013.12.037.

[42] R. Li, F. Xie, J. Liu, C. Zhang, X. Zhang, C. Fan, Room-temperature hydrolysis fabrication of BiOBr/$Bi_{12}O_{17}Br_2$ Z-Scheme photocatalyst with enhanced resorcinol degradation and NO removal activity, Chemosphere 235 (2019) 767–775, https://doi.org/10.1016/j.chemosphere.2019.06.231.

[43] X. Shi, P. Wang, W. Li, Y. Bai, H. Xie, Y. Zhou, L. Ye, Change in photocatalytic NO removal mechanisms of ultrathin BiOBr/BiOI via NO_3– adsorption, Appl. Catal. B Environ. 243 (2019) 322–329, https://doi.org/10.1016/j.apcatb.2018.10.037.

[44] Q. Wang, D. O'hare, Large-scale synthesis of highly dispersed layered double hydroxide powders containing delaminated single layer nanosheets, Chem Commun. 49 (2013) 6301–6303, https://doi.org/10.1039/c3cc42918k.

[45] J.M. Montoya-Zamora, A. Martínez-de la Cruz, E. López-Cuéllar, F.A. Pérez González, BiOBr photocatalyst with high activity for NO_x elimination, Adv. Powder Technol. 31 (2020) 3618–3627, https://doi.org/10.1016/j.apt.2020.07.009.

[46] W. Li, Y. Zou, X. Geng, F. Xiao, G. An, D. Wang, Constructing highly catalytic oxidation over BiOBr-based hierarchical microspheres: importance of redox potential of doped cations, Mol. Catal. 438 (2017) 19–29, https://doi.org/10.1016/j.mcat.2017.05.017.

[47] C. Zhao, Y. Liang, W. Li, X. Chen, Y. Tian, D. Yin, Q. Zhang, 3D BiOBr/BiOCl heterostructure microspheres with enhanced photocatalytic activity, J. Mater. Sci. Mater. Electron. 31 (2020) 1868–1878, https://doi.org/10.1007/s10854-019-02706-x.

[48] Y. Bi, Y. Wang, X. Dong, N. Zheng, H. Ma, X. Zhang, Efficient solar-driven conversion of nitrogen to ammonia in pure water: Via hydrogenated bismuth oxybromide, RSC Adv. 8 (2018) 21871–21878, https://doi.org/10.1039/c8ra02483a.

[49] W.W. Lee, C.S. Lu, C.W. Chuang, Y.J. Chen, J.Y. Fu, C.W. Siao, C.C. Chen, Synthesis of bismuth oxyiodides and their composites: characterization, photocatalytic activity, and degradation mechanisms, RSC Adv. 5 (2015) 23450–23463, https://doi.org/10.1039/c4ra15072d.

[50] K.A. Reyna-Cavazos, A.M. de la Cruz, F.E. Longoria Rodríguez, E. López-Cuellar, Synthesis of bismuth oxyiodide (BiOI) by means of microwaves in glycerol with high photocatalytic activity for the elimination of NO_x and SO_2, Res. Chem. Intermed. 46 (2020) 923–941, https://doi.org/10.1007/s11164-019-03998-8.

[51] M.C. Capel-Sanchez, G. Blanco-Brieva, J.M. Campos-Martin, M.P. De Frutos, W. Wen, J.A. Rodriguez, J.L.G. Fierro, Grafting strategy to develop single site titanium on an amorphous silica surface, Langmuir 25 (2009) 7148–7155, https://doi.org/10.1021/la900578u.

[52] P. Cruz, E.A. Granados, M. Fajardo, I. del Hierro, Y. Pérez, Heterogeneous oxidative desulfurization catalysed by titanium grafted mesoporous silica nanoparticles containing tethered hydrophobic ionic liquid: a dual activation mechanism, Appl. Catal. A Gen. 587 (2019), 117241, https://doi.org/10.1016/j.apcata.2019.117241.

[53] H. Search, C. Journals, A. Contact, M. Iopscience, I.P. Address, Defects and hyperfine interactions in Ni – Y intermetallics (Y= Al, Ga, In, Ti) via 27Al, 47Ti, 61Ni,69,71Ga and 115In nuclear resonance, J. Phy Condes. Matter. 15 (2003) 8389–8406, https://doi.org/10.1088/0953-8984/15/49/016.

[54] D. Padro, V. Jennings, M.E. Smith, R. Hoppe, P.A. Thomas, R. Dupree, Variations of titanium interactions in solid state NMR-correlations to local structure, J. Phys. Chem. B. 106 (2002) 13176–13185, https://doi.org/10.1021/jp021583x.

[55] P.J. Sideris, U.G. Nielsen, Z. Gan, C.P. Grey, Mg/Al ordering in layered double hydroxides revealed by multinuclear NMR spectroscopy, Science 321 (5885) (2008) 113–117.

[56] V. Vivier, C. Cachet-Vivier, S. Mezaille, B.L. Wu, C.S. Cha, J.-Y. Nedelec, M. Fedoroff, D. Michel, L.T. Yu, Electrochemical study of Bi_2O_3 and $Bi_2O_2CO_3$ by means of a cavity microelectrode. I. observed phenomena and direct analysis of results, J. Electrochem. Soc. 147 (2000) 4252, https://doi.org/10.1149/1.1394049.

[57] V.D. Nithya, R. Kalai Selvan, L. Vasylechko, C. Sanjeeviraja, Surfactant assisted sonochemical synthesis of Bi_2WO_6 nanoparticles and their improved electrochemical properties for use in pseudocapacitors, RSC Adv. 4 (2014) 4343–4352, https://doi.org/10.1039/c3ra44941f.

[58] V.D. Nithya, B. Hanitha, S. Surendran, D. Kalpana, R. Kalai Selvan, Effect of pH on the sonochemical synthesis of $BiPO_4$ nanostructures and its electrochemical properties for pseudocapacitors, Ultrason. Sonochem. 22 (2015) 300–310, https://doi.org/10.1016/j.ultsonch.2014.06.014.

[59] V. Vivier, A. Régis, G. Sagon, J.Y. Nedelec, L.T. Yu, C. Cachet-Vivier, Cyclic voltammetry study of bismuth oxide Bi_2O_3 powder by means of a cavity microelectrode coupled with Raman microspectrometry, Electrochim. Acta. 46 (2001) 907–914, https://doi.org/10.1016/S0013-4686(00)00677-0.

[60] P. Vialat, F. Leroux, C. Taviot-Gueho, G. Villemure, C. Mousty, Insights into the electrochemistry of $(Co_xNi_{(1-x)})_2Al\text{-}NO_3$ layered double hydroxides, Electrochim. Acta. 107 (2013) 599–610, https://doi.org/10.1016/j.electacta.2013.06.033.

[61] P. Vialat, F. Leroux, C. Mousty, Electrochemical properties of layered double hydroxides containing 3d metal cations, J. Solid State Electrochem. 19 (2015) 1975–1983, https://doi.org/10.1007/s10008-014-2671-0.

[62] M. Lovrić, F. Scholz, A model for the propagation of a redox reaction through microcrystals, J. Solid State Electrochem. 1 (1997) 108–113, https://doi.org/10.1007/s100080050030.

[63] K.B. Oldham, Voltammetry at a three-phase junction, J. Solid State Electrochem. 2 (1998) 367–377, https://doi.org/10.1007/s100080050113.

[64] M. Lovrić, F. Scholz, A model for the coupled transport of ions and electrons in redox conductive microcrystals, J. Solid State Electrochem. 3 (1999) 172–175, https://doi.org/10.1007/s100080050144.

[65] Y. Miao, Z. Yang, X. Liu, L. Xu, L. Ouyang, Y. Gu, H. Chang, R. Ouyang, Self-assembly of BiIII ultrathin layer on Pt surface for non-enzymatic glucose sensing, Electrochim. Acta. 111 (2013) 621–626, https://doi.org/10.1016/j.electacta.2013.07.188.

[66] S.T.U. Din, H. Lee, W. Yang, Z-Scheme heterojunction of 3-dimensional hierarchical Bi_3O_4Cl/Bi_5O_7I for a significant enhancement in the photocatalytic degradation of organic pollutants (RhB and BPA), Nanomaterials 12 (2022) 767, https://doi.org/10.3390/nano12050767.

[67] J. Ortiz-Bustos, I. del Hierro, Y. Pérez, Photocatalytic oxidative desulfurization and degradation of organic pollutants under visible light using TiO_2 nanoparticles modified with iron and sulphate ions, Ceram. Int. 48 (2022) 6905–6916, https://doi.org/10.1016/j.ceramint.2021.11.246.

[68] X. Cai, Y. Luo, B. Liu, H.M. Cheng, Preparation of 2D material dispersions and their applications, Chem Soc. Rev. 47 (2018) 6224–6266, https://doi.org/10.1039/c8cs00254a.

[69] C. Chen, A. Wangriya, J.C. Buffet, D. O'Hare, Tuneable ultra high specific surface area Mg/Al-CO_3 layered double hydroxides, Dalt. Trans. 44 (2015) 16392–16398, https://doi.org/10.1039/c5dt02641e.

[70] Y. Zhao, P. Chen, B. Zhang, D.S. Su, S. Zhang, L. Tian, J. Lu, Z. Li, X. Cao, B. Wang, M. Wei, D.G. Evans, X. Duan, Highly dispersed TiO_6 units in a layered double hydroxide for water splitting, Chem - A Eur. J. 18 (2012) 11949–11958, https://doi.org/10.1002/chem.201201065.

[71] B. Li, Y. Zhao, S. Zhang, W. Gao, M. Wei, Visible-light-responsive photocatalysts toward water oxidation based on NiTi-layered double hydroxide/reduced graphene oxide composite materials, ACS Appl. Mater. Interfaces. 5 (2013) 10233–10239, https://doi.org/10.1021/am402995d.

[72] R.S. Wade, C.E. Castro, Reactions of oxymyoglobin with NO, NO_2, and NO_2^- under argon and in air, Chem Res. Toxicol. 9 (1996) 1382–1390, https://doi.org/10.1021/tx9600457.

[73] F. Rodriguez-Rivas, A. Pastor, C. Barriga, M. Cruz-Yusta, L. Sánchez, I. Pavlovic, Zn-Al layered double hydroxides as efficient photocatalysts for NO_x abatement, Chem Eng. J. 346 (2018) 151–158, https://doi.org/10.1016/j.cej.2018.04.022.

[74] A. Nehdi, N. Frini-Srasra, G. de Miguel, I. Pavlovic, L. Sánchez, J. Fragoso, Use of LDH- chromate adsorption co-product as an air purification photocatalyst, Chemosphere 286 (2022), https://doi.org/10.1016/j.chemosphere.2021.131812.

[75] J. Balbuena, J.M. Calatayud, M. Cruz-Yusta, P. Pardo, F. Martín, J. Alarcón, L. Sánchez, Mesocrystalline anatase nanoparticles synthesized using a simple

hydrothermal approach with enhanced light harvesting for gas-phase reaction, Dalt. Trans. 47 (2018) 6590–6597, https://doi.org/10.1039/c8dt00721g.
[76] Y. Zhao, B. Li, Q. Wang, W. Gao, C.J. Wang, M. Wei, D.G. Evans, X. Duan, D. O'Hare, NiTi-Layered double hydroxides nanosheets as efficient photocatalysts for oxygen evolution from water using visible light, Chem Sci. 5 (2014) 951–958, https://doi.org/10.1039/c3sc52546e.
[77] P. Chen, H. Liu, Y. Sun, J. Li, W. Cui, L. Wang, W. Zhang, X. Yuan, Z. Wang, Y. Zhang, F. Dong, Bi metal prevents the deactivation of oxygen vacancies in $Bi_2O_2CO_3$ for stable and efficient photocatalytic NO abatement, Appl. Catal. B Environ. 264 (2020), 118545, https://doi.org/10.1016/j.apcatb.2019.118545.
[78] J. Liao, W. Cui, J. Li, J. Sheng, H. Wang, X. Dong, P. Chen, G. Jiang, Z. Wang, F. Dong, Nitrogen defect structure and NO^+ intermediate promoted photocatalytic NO removal on H_2 treated g-C_3N_4, Chem Eng. J. 379 (2020), 122282, https://doi.org/10.1016/j.cej.2019.122282.
[79] W. Huo, W. Xu, T. Cao, Z. Guo, X. Liu, G. Ge, N. Li, T. Lan, H.C. Yao, Y. Zhang, F. Dong, Carbonate doped Bi_2MoO_6 hierarchical nanostructure with enhanced transformation of active radicals for efficient photocatalytic removal of NO, J. Colloid Interface Sci. 557 (2019) 816–824, https://doi.org/10.1016/j.jcis.2019.09.089.
[80] X. Li, W. Zhang, W. Cui, J. Li, Y. Sun, G. Jiang, H. Huang, Y. Zhang, F. Dong, Reactant activation and photocatalysis mechanisms on Bi-metal@Bi_2GeO_5 with oxygen vacancies: a combined experimental and theoretical investigation, Chem Eng. J. 370 (2019) 1366–1375, https://doi.org/10.1016/j.cej.2019.04.003.
[81] W. Zhang, X. Dong, Y. Liang, Y. Sun, F. Dong, Ag/AgCl nanoparticles assembled on BiOCl/$Bi_{12}O_{17}Cl_2$ nanosheets: Enhanced plasmonic visible light photocatalysis and in situ DRIFTS investigation, Appl. Surf. Sci. 455 (2018) 236–243, https://doi.org/10.1016/j.apsusc.2018.05.171.
[82] W. Huo, W. Xu, T. Cao, X. Liu, Y. Zhang, F. Dong, Carbonate-intercalated defective bismuth tungstate for efficiently photocatalytic NO removal and promotion mechanism study, Appl. Catal. B Environ. 254 (2019) 206–213, https://doi.org/10.1016/j.apcatb.2019.04.099.
[83] W. Huo, T. Cao, W. Xu, Z. Guo, X. Liu, H.C. Yao, Y. Zhang, F. Dong, Facile construction of $Bi_2Mo_3O_{12}$@$Bi_2O_2CO_3$ heterojunctions for enhanced photocatalytic efficiency toward NO removal and study of the conversion process, Chinese J. Catal. 41 (2020) 268–275, https://doi.org/10.1016/S1872-2067(19)63460-1.
[84] Y. Xin, Q. Zhu, T. Gao, X. Li, W. Zhang, H. Wang, D. Ji, Y. Huang, M. Padervand, F. Yu, C. Wang, Photocatalytic NO removal over defective Bi/BiOBr nanoflowers: the inhibition of toxic NO_2 intermediate via high humidity, Appl. Catal. B Environ. 324 (2023), 122238, https://doi.org/10.1016/j.apcatb.2022.122238.
[85] H. Li, H. Zhu, Y. Shi, H. Shang, L. Zhang, J. Wang, Vacancy-rich and porous NiFe-layered double hydroxide ultrathin nanosheets for efficient photocatalytic NO oxidation and storage, Environ. Sci. Technol. 56 (2022) 1771–1779, https://doi.org/10.1021/acs.est.1c07811.